Mineralium Deposita (2019) 54:193–216
https://doi.org/10.1007/s00126-018-0830-4

ARTICLE

The Hämmerlein skarn-hosted polymetallic deposit and the Eibenstock granite associated greisen, western Erzgebirge, Germany: two phases of mineralization—two Sn sources

Marie G. Lefebvre[1] · Rolf L. Romer[1] · Johannes Glodny[1] · Uwe Kroner[2] · Marco Roscher[3]

Received: 8 January 2018 / Accepted: 23 July 2018 / Published online: 9 August 2018

Abstract

The Hämmerlein polymetallic deposit is hosted in skarn, schists, and gneisses that reached their metamorphic peak at ~ 340 Ma during the Variscan orogeny. The deposit is spatially closely associated with one of the most voluminous granites of the Erzgebirge, the Eibenstock granite which intruded the metamorphic units at ~ 320 Ma, and locally also developed greisen mineralization. Cassiterite is the main ore mineral in the Hämmerlein skarn and in greisen mineralizations associated with the Eibenstock granite. The age of skarn formation is bracketed by multi-mineral Rb-Sr isochron ages of the gneisses (~ 340 Ma) and the end of ductile deformation (> 330 Ma). The dated calc-silicate minerals of the skarn have elevated Sn contents, which implies that some Sn was present in the system during regional metamorphism, i.e., well before the emplacement of the Eibenstock granite. Tin in the > 330 Ma old skarn silicates possibly was mobilized from the metamorphic wall rocks. Retrogression of the skarn mineral assemblage may have released some Sn that formed cassiterite in an assemblage with chlorite and fluorite. The Sr isotope signatures of fluorite indicate that this late assemblage is not related to cooling of the metamorphic rocks, but to the emplacement of the Eibenstock granite, which introduced additional Sn into the skarn. Thus, mineralization in the Hämmerlein deposit includes Sn that was introduced during two different events from different sources.

Keywords Erzgebirge · Hämmerlein · Tin · Skarn · Greisen · Ore deposits · Eibenstock granite

Introduction

The Hämmerlein polymetallic skarn deposit is located in the western Erzgebirge, in the northern part of the Bohemian Massif. The area is dominated by schists and gneisses that mostly represent Cambro-Ordovician sedimentary protoliths, metamorphosed at ~ 340 Ma during the Variscan orogeny. The Hämmerlein mineralization is hosted in a unit that formerly was referred as Jáchymov Group and that includes mica-schists with skarns, gneisses, and amphibolites. The high-pressure–low temperature metamorphic units are intruded by the S-type, high-F, high-P_2O_5 Li-mica Eibenstock granite, which is exposed to the west of the deposit. Hämmerlein was discovered in the course of uranium mining activities and prospected during the second half of the twentieth century not only for tin but also for indium and zinc. The current resource estimation for Hämmerlein is 101,500-t Sn with a cutoff grade of 0.2-wt% Sn. Indium and zinc contents have also been estimated at 2149 and 200,200 t, respectively.

Most earlier studies focused mainly on the ore minerals and their deposition at Hämmerlein (Malyshev and Korzhanovskaya 1989; Shapenko and Šmidel 1991; Malyshev et al. 1997), but there are no studies on the skarn formation itself. Based on petrographic observations, mineral and bulk rock chemistry, P-T-XCO_2 modeling, and Rb-Sr dating, the aim of this study is to understand whether the regional

Editorial handling: R. Linnen

Electronic supplementary material The online version of this article (https://doi.org/10.1007/s00126-018-0830-4) contains supplementary material, which is available to authorized users.

✉ Marie G. Lefebvre
lefebvre@gfz-potsdam.de

[1] Deutsches GeoForschungsZentrum GFZ, Telegrafenberg, 14473 Potsdam, Germany

[2] Department of Geology, TU Bergakademie Freiberg, B.-v. -Cotta-Str. 2, D-09596 Freiberg, Germany

[3] Saxore Bergbau GmbH, Burgstr. 19, 09599 Freiberg, Germany

metamorphism or the Eibenstock granite intrusion is responsible of the skarn formation, when in its history the mineralization took place, and where exactly the tin was preferentially deposited. We demonstrate that the Hämmerlein skarn formed during the Variscan regional metamorphism and that it was later overprinted during the intrusion of the Eibenstock granite. Furthermore, we demonstrate that Sn was incorporated into the skarn during its formation and was redistributed during the emplacement of the granite along with a new input of Sn into the skarn. Greisen mineralization is directly related to the emplacement of the Eibenstock granite.

Geological setting

Tectonic context

The Variscan orogenic belt formed by the collision of Laurussia with Gondwana in the late Paleozoic (Franke 1989; Matte 1986), starting with the closure of the Rheic Ocean (collision of Armorica and the Teplá-Barrandian Unit with Laurussia) and followed by intra-continental subduction of thinned continental crust and its sedimentary cover (Kroner and Romer 2013). In the Bohemian Massif, these deeply subducted continental rocks reached peak metamorphic conditions at about 340 Ma (Rötzler et al. 1998) and eventually were emplaced into the middle and upper crust, where they form high-strain belts of metamorphic nappes (Kroner and Romer 2013). The Erzgebirge in the Saxo-Thuringian Zone of the Variscan orogeny (Fig. 1a) is part of the allochthonous domain (Kroner et al. 2007) and represents a stack of medium to ultra-high pressure metamorphic nappes that were rapidly exhumed (Rötzler and Plessen 2010). The metamorphic nappes have been intruded by a wide range of geochemically contrasting post-kinematic granites, some of which show closely-associated important tin mineralization (Förster et al. 1999).

The metamorphic nappes of the Erzgebirge are dominated by rocks of the former Gondwana margin (Mingram 1998) that have been subducted and exhumed during the early Carboniferous (Willner et al. 1997; Rötzler et al. 1998). The former Gondwana margin consisted of a Cadomian basement with important Cambrian granodiorites (Linnemann et al. 2004) and early Ordovician magmatic complexes (Tichomirowa and Leonhardt 2010) and its Cambro-Ordovician to Silurian volcanosedimentary cover units. These basement units and their volcanosedimentary cover behaved differently during the Variscan orogeny: (i) the basement rocks were subducted to medium-pressure conditions and are now exposed in the gneiss domes of the Erzgebirge. The tectonostratigraphically lowermost units are exposed in the eastern Erzgebirge (Freiberg Gneiss Dome) and are dominated by granodioritic orthogneisses derived from a ~ 550-Ma old protolith (Kröner et al. 1995). The medium pressure units of the Reitzenhain Gneiss Dome in the central Erzgebirge are sandwiched between nappes that experienced higher grade metamorphism during the Variscan orogeny. The Reitzenhain gneisses have protolith ages of c. 490 Ma (Tichomirowa and Leonhardt 2010). (ii) The volcanosedimentary cover rocks are dominated by Paleozoic protoliths (conglomerates, greywackes, pelites, marbles, rhyolites, and metabasites) (Rötzler and Plessen 2010). The various nappes reached peak conditions at ~ 340 Ma and became rapidly exhumed to middle and upper crustal levels. This is indicated by the emplacement of the 325- to 318-Ma old post-kinematic granites, which formed in the middle crust and were emplaced in the upper crust (< 2 kbar) (Förster et al. 1999).

There are three age groups of granitic rocks: (i) 340–330-Ma old intrusions (Meissen, Berbersdorf) along crustal scale shear zones and in contact with UHT metamorphic units were emplaced synchronous with the emplacement of the metamorphic nappes (Förster and Romer 2010; Wenzel et al. 1997); (ii) 325–318-Ma old post-kinematic granitic intrusions (e.g., Eibenstock, Kirchberg) represent crustal melts and derive their geochemical variability from the lithologic and geochemical heterogeneity of the stacked continental crust (Förster et al. 1999; Förster and Romer 2010); and (iii) 305–280-Ma old intrusions and volcanic complexes (Gottesberg) with variable input of mantle-derived material are bound to extensional structures of the Central European Extensional Province that developed in response to reorganization of the regional stress field after the Variscan orogeny (Kroner and Romer 2013; Kroner et al. 2016). Most tin and tungsten mineralization of the Erzgebirge is thought to be related to 325–318-Ma old granites (Förster et al. 1999) that formed by melting of quartzo-feldspathic rock mixed with micaceous metapelite enriched in Sn and W (Breiter 2012).

Post-kinematic granites

The 325–318-Ma-old post-kinematic granites are classified in three groups: (1) low-F biotite granites (Kirchberg), (2) low-F two-mica granites (Fichtelgebirge), and (3) high-F, high-P_2O_5 Li-mica granites (Eibenstock) (Förster et al. 1999; Förster and Romer 2010). The composite Eibenstock granite is the "type" pluton for the high-F, high-P_2O_5 Li-mica granites. This granite commonly is mainly equigranular, but may locally show a porphyritic texture with a coarse grained assemblage with K-feldspar and minor quartz phenocrysts (Förster et al. 1999). There are no significant differences in the chemical composition between porphyric and non-porphyric varieties.

The Eibenstock granite constitutes the northern part of the Eibenstock-Nejdek pluton (Breiter 1993), a 25 by 22-km large complex in the western Erzgebirge (Fig. 1a). This complex is the most voluminous granitic body of the Erzgebirge, and it was emplaced in a late/post-collisional regime into paragneisses and schists, i.e., medium- and low-grade metamorphic rocks of the nappe pile of the Erzgebirge (Förster et al. 1999).

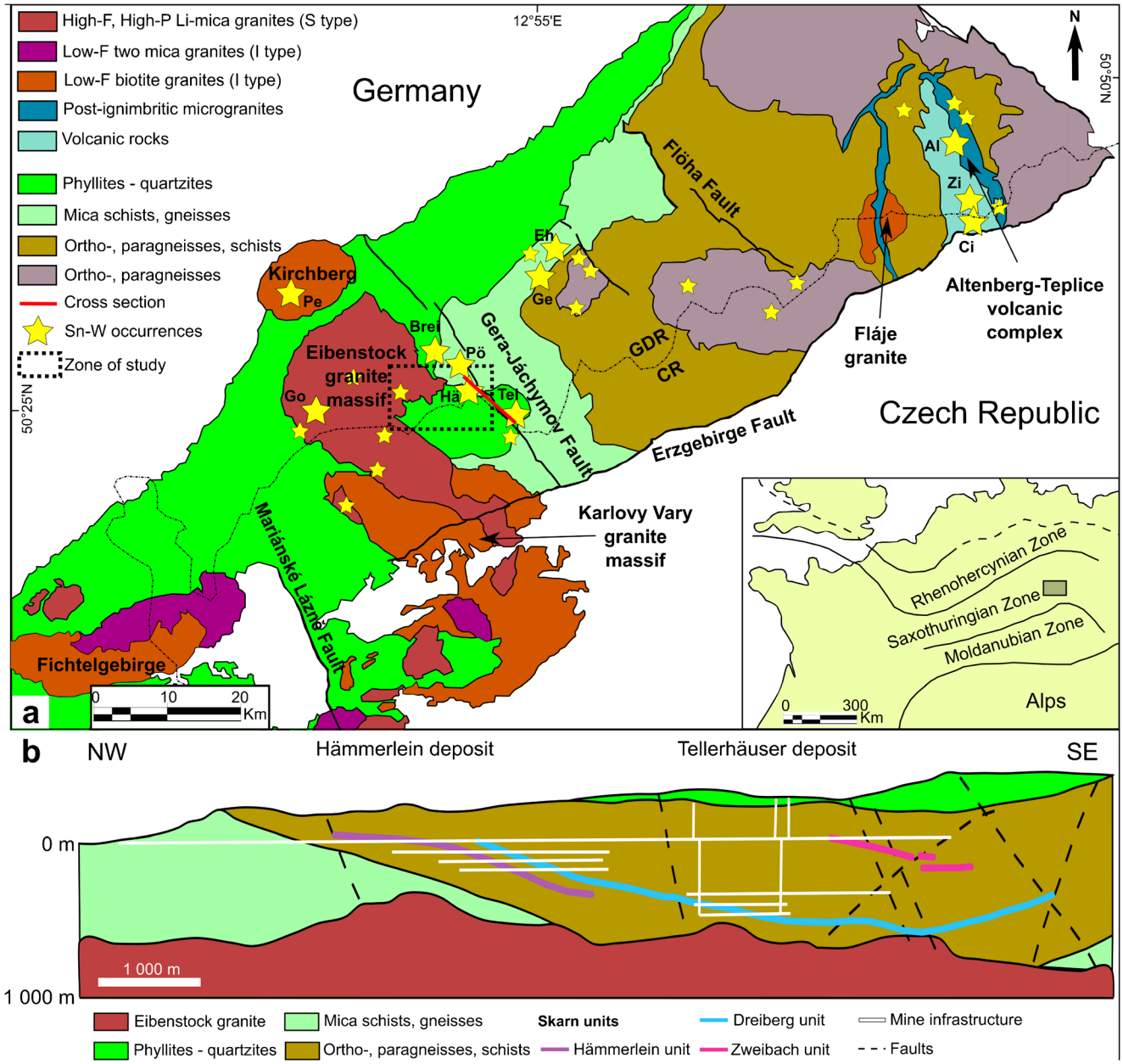

Fig. 1 **a** Simplified geological map of the Erzgebirge-Vogtland-Fichtelgebirge area showing the distribution of the various tin and tungsten deposits. Most of the ore deposits are spatially associated with granites (deposit locations according to Štemprok and Blecha 2015. Al: Altenberg, Brei: Breitenbrunn, Ci: Cínovec/Zinnwald, Eh: Ehrenfriedersdorf, Ge: Geyer, Go: Gottesberg, Hä: Hämmerlein, Pe: Pechtelsgrün, Pö: Pöhla-Globenstein, Tel: Tellerhäuser). Insert: Domains of the Variscan orogen in Central Europe. **b** Simplified cross-section of the Hämmerlein-Tellerhäuser deposit; modified after Schuppan and Hiller (2012) and Anglo Saxony Mining (2015)

The granite is Si-rich, peraluminous, reduced, and has a crustal isotopic signature (Sr_i values range from 0.711 to 0.713, Velichkin et al. 1994) and is associated with Sn-W mineralization (Förster et al. 1999). The Paleozoic metamorphic units (gneisses, mica schists) have played a role in the formation of the granite (Breiter et al. 1999). The Eibenstock granite is a multi-stage granite intrusion, which have been dated between ~320 Ma (U-Pb dating by Förster 1998; Pb-Pb dating on zircon by Kempe et al. 2004) for the major part of the granite and ~310 Ma (U-Pb dating on zircon by Tichomirowa et al. 2016) for some younger intrusions.

There are two types of mica in this granite. The trioctahedral ones are rich in Li and Fe and accompanied by topaz. Dioctahedral Li-rich micas typically overgrow trioctahedral micas and feldspars. Accessory minerals include schorl, topaz, apatite, rutile, and zircon. Rutile may host several wt% of Ta, Nb, Sn, and W. In addition, the Eibenstock granite locally also has cassiterite, scheelite, and wolframite (Förster et al. 1999).

Skarn and greisen assemblages

Skarn assemblage

The Hämmerlein deposit is a polymetallic skarn, hosted in the metasedimentary rocks of the Erzgebirge nappe pile, which is intruded by a suite of post-kinematic granites and eventually overprinted by the late- to post-orogenic Gera-Jáchymov fault zone (Fig. 2). This NW-SE striking, recurrently reactivated fracture zone is causally related with major uranium mineralizations of the region (Schuppan and Hiller 2012). The Hämmerlein host rocks are dominated by schists (Shapenko and Šmidel 1991) that are intercalated with layers of metacarbonates affected by the skarn formation, amphibolites, gneisses, quartzitic, and carbon-rich schists (Schuppan and Hiller 2012) (Fig. 1b). Although metacarbonates are seen as the protolith for the skarn formation (Schuppan and Hiller 2012), it is worth noting that there are no relics of metacarbonates within the skarn layers. The foliated skarn is in tectonic contact with intensively deformed quartz-rich mica schists and gneisses (Fig. 3). The mica schists contain layers with tin-rich biotite (up to 0.1%) (Malyshev et al. 1997; Malyshev and Korzhanovskaya 1989). The metamorphic wall rocks of the Hämmerlein deposit form the roof of the Eibenstock intrusion (Fig. 1b).

There are three types of mineralization in the Hämmerlein deposit: (i) skarn with magnetite mineralization, (ii) skarn with strata-bound tin and sulfide mineralization (mainly sphalerite), and (iii) hydrothermal uranium-bearing veins (Schuppan and Hiller 2012). Skarn mineralization is controlled by SW-NE striking faults (Schuppan and Hiller 2012). In contrast, hydrothermal uranium mineralization is connected with N-S and NW-SE striking faults and is related to multiple reactivations of the Gera-Jáchymov zone at 280 Ma and later (Förster 1996). The source of Sn in the skarn deposit has been enigmatic. Even though a close spatial relation has been established between the greisen deposits and granite, the relation between skarn Sn mineralization and granite is less clear. The granite and the skarn are close together (Fig. 1b), but there is no contact between them.

There are four types of skarn at Hämmerlein, garnet skarn, amphibole skarn, pyroxene skarn, and magnetite skarn that show different successions at different locations of the deposit (Table 1). The three calc-silicate skarns are microcrystalline and the most obvious difference between them is the color of their matrix, which depends on their content of garnet (brownish-red matrix for the garnet skarn), amphibole (grayish-green for the amphibole skarn), and pyroxene (light brownish-green for the pyroxene skarn). The fourth type of skarn is a magnetite skarn which is mainly composed of massive magnetite partially

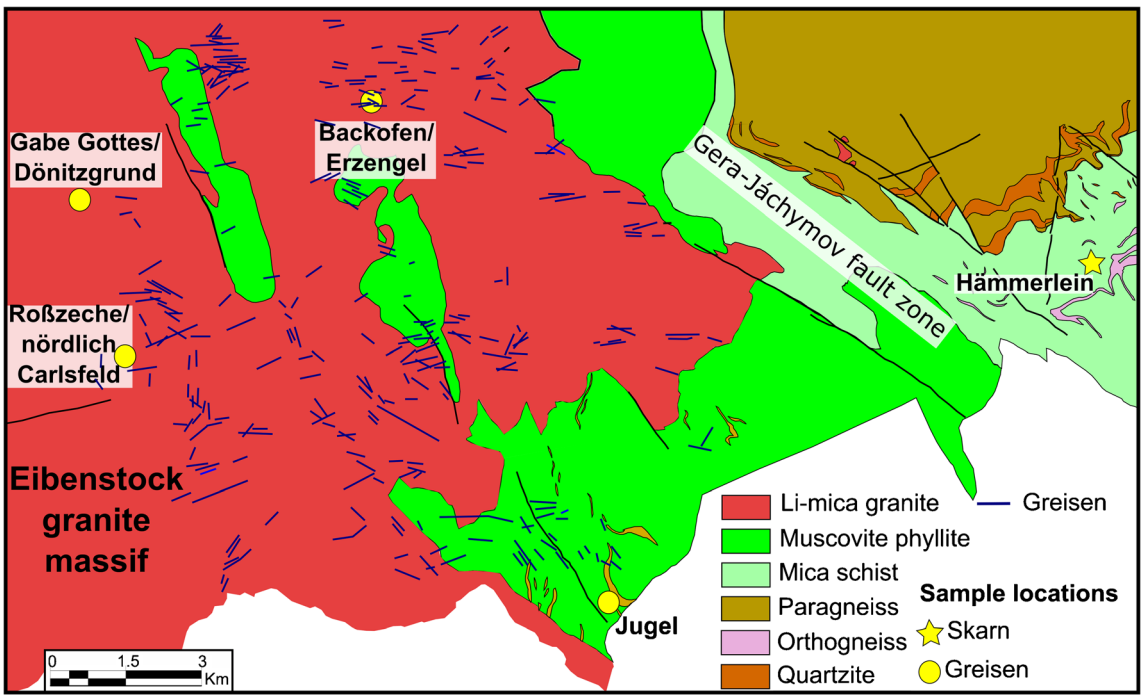

Fig. 2 Simplified geological map of the studied area showing the location of Hämmerlein and the locations of the dated greisen samples. The Hämmerlein deposit is hosted in micaschists, whereas greisen mineralizations are located along faults within the muscovite phyllite unit or within the Eibenstock granite (modified after Leonhardt et al. 1999, 2004, 2010)

interspersed with irregular, up to 5-cm large patches of chalcopyrite.

Garnet skarn (samples HAS2 and HGS1) is mainly composed of garnet and quartz. Garnet crystals are still visible in the amphibole skarn where the two skarn types are in contact (Fig. 4a). Garnet does not seem to be altered into chlorite, whereas coexisting amphibole is strongly altered. At the contact with gneiss, some muscovite and strongly chloritized biotite occur in the garnet skarn. Chlorite that formed by the alteration of biotite typically is associated with apatite.

Amphibole skarn (samples HAS1, HAS2, and HAS3) is mainly composed of chloritized amphibole, quartz, and some rare feldspar. Some relics of calcite are surrounded by amphibole (Fig. 4b) showing that calcite was a precursor phase for the skarn formation. As feldspar crystals are rare and strongly altered, they may reflect early phases or be inherited from the protolith. Amphibole and quartz formed from this protolith during the prograde stage of the skarn formation. Chlorite occurs along grain boundaries, as pseudomorphs after amphibole, and in veinlets, where it is associated with tourmaline and rare muscovite. Chlorite alteration and late veins of muscovite-tourmaline are not part of the skarn assemblage, but reflect a later event of retrogression or alteration. In contrast, apatite occurs mainly as inclusions in feldspar crystals, which are remnants of the protolith, and, thus apatite may have formed at the same time as feldspar and be inherited from the protolith. Cassiterite occurs in two different forms: (i) coarse grained cassiterite (up to 10 mm) at the contact between chloritized amphibole and magnetite (at contact to the magnetite skarn, e.g., sample HAS2) and (ii) fine-grained cassiterite (~ 10 μm) that is disseminated in the amphibole-quartz assemblage. Both types of cassiterite are associated with chlorite. Cassiterite formed during the later retrogression or alteration event that also led to the chloritization of the original skarn minerals.

Pyroxene skarn (sample CSV1) is mainly composed of pyroxene crystals (Fig. 4c) and recrystallized quartz with some rare bigger crystals of feldspar and quartz. At the contact between pyroxene skarn and gneiss, pyroxene forms altered veinlets in the gneiss (e.g., sample CSV1). Fractures within the gneiss may contain elongate crystals of muscovite which are accompanied by small apatite crystals. Muscovite and apatite seem to have formed later than pyroxene as they occur in fractures that locally cut the pyroxene veinlets. Locally, pyroxene skarn and gneiss are closely interbedded, forming a rock (e.g., sample HPS1) that is mainly composed of quartz and feldspar associated with small pyroxene crystals. Lenses of bigger pyroxene typically are surrounded by quartz. Veins of calcite cut both the quartz-feldspar assemblage and lenses of pyroxene, thus, showing that calcite formed as a retrograde phase, whereas pyroxene is part of the prograde assemblage.

The magnetite skarn is mainly composed of massive magnetite that is variably martitized at the rim of the crystals. There are irregular patches of chalcopyrite and pyrite within the magnetite (sample HMS1). Chalcopyrite may bear exsolutions of In-sphalerite (Fig. 4d). Minor arsenopyrite and Bi-Cu minerals occur disseminated in the magnetite skarn. Late fractures in the rock contain quartz and chlorite.

The textural relation between skarn and gneisses is complex, due to the overprinting of older structures by younger ones and the contrasting rheological behavior of gneisses, schists, and skarn. The regional metamorphic layering is characterized by pervasive foliated metasedimentary rocks and foliated skarn incorporating lenses of orthogneiss. Within the ductile deformed gneiss, there are local granitic segregations along fractures that crosscut the older foliation of the gneiss (Fig. 3a). These local granitic segregations may reflect fluid channels and possibly formed due to local fluid-overpressure near metamorphic peak conditions. Fluid overpressure led to the formation of a second fracture system with associated amphibole skarn within the gneiss partly reactivating the first fractures (Fig. 3a). Amphibole skarn that cuts the foliation of the gneisses is not foliated, whereas amphibole skarn at the margin of gneiss lenses is pervasively foliated. Pervasive deformation of amphibole skarn is concentrated outside of the gneiss, because of the viscosity contrast between the skarn (low viscosity) and the gneiss (higher viscosity). Hence, the subparallel foliations of the gneiss and the skarn reflect two distinct synmetamorphic, deformational events interrupted by brittle fracturing. The various skarns and the two fracture systems developed when the entire sequence still was in the temperature field of ductile deformation. A third fracture system cutting across the entire metasedimentary sequence evolved in the brittle upper crust and contains significant hydrothermal tin mineralization. Because cooling of the Erzgebirge below the ductile-brittle transition occurred no later ca. 330 Ma (e.g., Werner and Lippolt 2000), the formation of ductile-deformed amphibole skarn as well as related fractures is distinctly older than the emplacement of the post-kinematic intrusion of the Eibenstock granite and the associated youngest fractures (Fig. 3e).

Greisen assemblage

Sn-greisens are generally located within or close to the Eibenstock granite (Fig. 2). The greisen formed after the coarse-grained phase of the granite (Rojík 2005). Tin-bearing greisens typically not only are concentrated along the granite margin but also occur along SE-striking zones within the Eibenstock granite. Greisens cut all textural types of Eibenstock granite. Tin mineralization rarely crosses the outer contact of the granite (Rojík 2005).

Greisens follow short subvertical joints and form grouped bands separated into parallel-packed zones. The center of the greisen typically is mineralized with cassiterite veinlets. The

main greisen mineralization includes several generations of greisen with higher ore grades at the contacts.

There are several types of greisen (Table 1). All of them are composed of quartz and fine-grained mica with disseminated strongly altered feldspar. The various greisen occurrences mainly differ in the nature of accessory minerals. The samples from Backofen, Erzengel, and Gabe Gottes (BO1, EE2, and GG1, respectively; Fig. 2) show two types of white mica: (i) up to 2-cm large ferroan poly-lithionite phenocrysts associated with feldspar and quartz phenocrysts, which seem to be remnants of the primary granite, and (ii) fine-grained second generation, up to 200-μm large alteration-related muscovite crystals at the boundaries of feldspar and ferroan poly-lithionite phenocrysts. Sample GG3 (Gabe Gottes) does not show ferroan poly-lithionite phenocrysts, but only fine-grained mica. In this sample, phenocrysts seem to have been altered completely and the only mica present belongs to the second generation. Cassiterite forms ~ 250-μm large crystals that occur together with second-generation mica (Fig. 5b). Cassiterite may have formed at the same time as the alteration that formed the second generation of mica. Samples from the Jugel metasomatized phyllite (JG1 and JG2) show the assemblage muscovite-tourmaline-cassiterite in fractures within a quartz-feldspar assemblage. Muscovite forms small fan-shaped grains and tourmaline crystals reach up to 500 μm (Fig. 5c). Locally, there is up to 200-μm large apatite (sample EE2, Fig. 5a) together with second generation muscovite. The assemblage muscovite-tourmaline-apatite-cassiterite reflects a late-stage event that also resulted in the almost complete chloritization of biotite.

Mineralized veins associated with the greisen show coarse-grained aggregates of cassiterite in the center together with löllingite, arsenopyrite, wolframite, sericite, topaz, minor pyrite, fluorite, and rare feldspar. There are also veinlets between greisen bands with a similar mineral assemblage. They contain cassiterite, hematite, K-feldspar, quartz, wolframite, topaz, fluorite, and muscovite (Rojík 2005).

Materials and methods

Mineral compositions were determined using a JEOL Hyperprobe JXA-8500F at GFZ Potsdam. Natural and synthetic standards were used for the calibration. Analyses were performed with an accelerating voltage of 15 kV, beam current of 12 nA, and a beam diameter of 5 μm.

Mineral separation has been carried out for Rb-Sr and U-Pb analysis. Mineral concentrates of white mica, K-feldspar, albite, amphibole, garnet, apatite, tourmaline, epidote, sulfides, and fluorite were produced. The first crushing was performed in a steel mortar. Mineral enrichment has been done with a FRANTZ magnetic separator and heavy liquids. White mica fractions sieved to different size ranges had been grounded in pure ethanol in an agate mortar and then sieved again to remove adherent matrix and inclusions. All separates had been checked and purified by hand-picking. For Rb-Sr analysis, mineral separates had been spiked with mixed ^{87}Rb-^{84}Sr tracers to determine Rb and Sr concentrations. Rb-Sr and U-Pb data were measured on a TRITON multicollector thermal ionization mass spectrometer (TIMS) at GFZ Potsdam following the routine described in Glodny et al. (2002) and Romer and Hahne (2010), respectively.

Fig. 3 Tectonic evolution of the synmetamorphic skarn of the Hämmerlein deposit. **a** Lenses of gneiss mantled by pervasively foliated amphibole/pyroxene skarn layers are part of the metasedimentary/metavolcanic suite of the Erzgebirge nappe pile. Two fracture systems transect the foliation of the gneiss. The older fractures contain granitic segregations and were cut and partly reactivated by tension gashes containing unfoliated skarn. **b** Crosscutting relationship of the foliated skarn and the fracture system I indicating that the foliation of the skarn is younger than both the fractures and the foliation of the gneiss. **c** Emplacement of the skarn utilizing fracture system 2. This indicates a high viscosity contrast between the skarn and the gneiss as well as fluid overpressure. The skarn inside the gneiss is protected from the subsequent ductile deformation affecting the skarn mantle of the gneiss lenses, which remains under low differential stress at this stage. The fluid overpressure led to the formation of tension gashes and the subsequent emplacement of the low viscosity skarn. **d** After cooling of the metasedimentary sequence, a third generation of fractures crosscuts the entire sequence and is related to chloritization of the wall rock. **e** Schematic sketch of the formation of the synmetamorphic skarn layers. **e-I** Early Paleozoic sediments (siliciclastic and carbonate rocks) are intruded by dikes and sills. **e-II** Subsequent regional metamorphic overprint due to nappe stacking during the Variscan continental collision led to medium grade metamorphism and a pervasive deformation of the lithologies. Competence contrast between the orthogneisses and the metasediments resulted in pinch and swell structures in the gneiss. Fluid overpressure probably caused the formation of the oldest fractures with granitic segregations. **e-III** Due to the viscosity contrast between gneiss and the surrounding lithologies ongoing ductile deformation is localized in the metasediments including the evolving skarn layers. The gneiss preserves earlier deformation increments, i.e., the gneiss foliation as well as the granitic dikes. Fluid overpressure in combination with low differential stress inside gneiss culminated in the formation of a second fracture system. The emplacement of the skarn inside the gneiss indicates low viscosity of the skarn at this stage. **e-IV** A third fracture system postdates the metamorphic processes and is related to hydrothermal processes associated with the intrusion of the Eibenstock granite below the metasediments. Abbreviations: f—foliated skarn; u—unfoliated skarn; i, ii, iii—fracture systems 1–3

Results

Mineral chemistry

The greisen samples contain one generation of small fan-shaped white mica, except for samples from Backofen, Erzengel, and Gabe Gottes (BO1, EE2, and GG1,

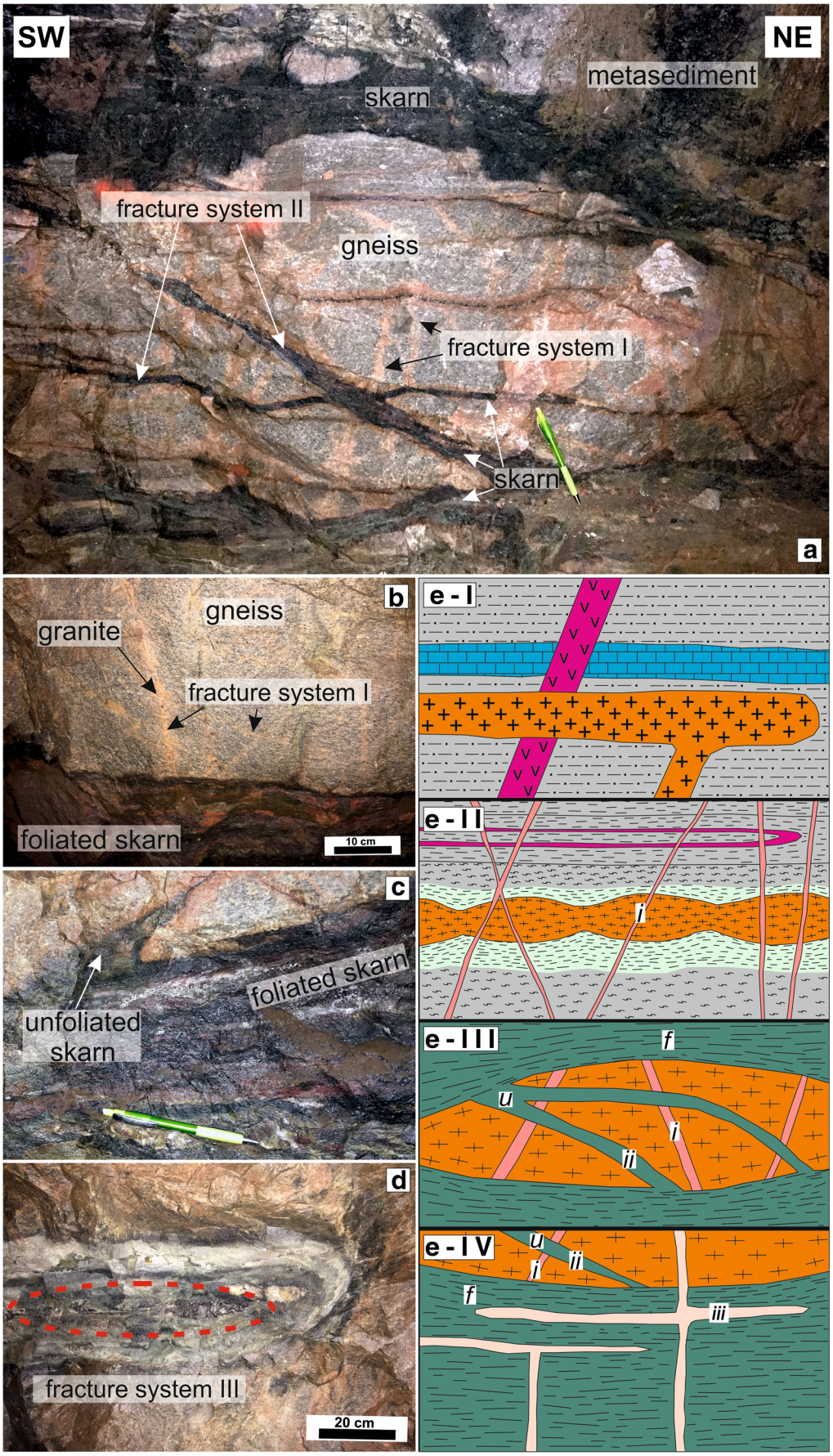
SW
NE
metasediment
skarn
fracture system II
gneiss
fracture system I
skarn
a
b
gneiss
granite
fracture system I
foliated skarn
10 cm
c
foliated skarn
unfoliated skarn
d
fracture system III
20 cm
e - I
e - II
i
e - III
f
u
i
ii
e - IV
u
ii
i
f
iii

Table 1 Description of the skarn samples from Hämmerlein and of the greisen associated to the Eibenstock granite (skarn samples location in Gauss-Krüger coordinates, zone 4)

Sample name	Lithology	Location	Characteristics
Hämmerlein skarn samples			
CSV1	Contact between pyroxene skarn and gneiss	5 593 093 mN 4 559 547 mE	This sample is mainly composed of prograde pyroxene and recrystallized quartz. Rare bigger altered crystals of quartz and feldspar are visible. In the gneiss, pyroxene forms veinlets. Elongate crystals of muscovite together with apatite occur within fractures cutting pyroxene veinlets.
ASb, HAS2	Contact between garnet and amphibole skarns	5 593 125 mN 4 559 500 mE	Samples are formed by chloritized amphibole and quartz. Some garnet and rare feldspar crystals occur within the prograde amphibole-quartz assemblage. Clusters of green amphibole surrounding remnant calcite also occur. Cassiterite occurs at contacts between chloritized amphibole and magnetite as coarse grains (up to 10 mm).
HAS3	Contact between amphibole skarn and gneiss	5 593 194 mN 4 559 409 mE	This sample is similar to sample HAS2 but here smaller cassiterite (~ 10 μm) occurs disseminated in the skarn prograde assemblage and is associated with chlorite.
HGS1	Contact between garnet and amphibole skarn	5 593 000 mN 4 559 500 mE	The garnet skarn is composed of prograde garnet and quartz crystals. In the amphibole skarn, some secondary chlorite also occurs in the skarn in association with apatite.
HMS1	Magnetite skarn	5 593 000 mN 4 559 500 mE	The main component of the sample is variably martitized massive magnetite. Patches of chalcopyrite and pyrite occur in the magnetite. Indium-sphalerite exsolutions appear in chalcopyrite.
HPS1	Contact between pyroxene and amphibole skarn	5 593 000 mN 4 559 500 mE	The pyroxene skarn is mainly composed of prograde pyroxene and quartz crystals. Some lenses of coarse pyroxene (~ 1 cm) occur in the pyroxene-quartz assemblage. Some secondary calcite veinlets crosscut both the matrix and the lenses.
Greisen samples			
BO1	Granite	Backofen/Sosa	Two types of mica occur in a matrix mainly composed of quartz. Ferroan polz-lithionite phenocrysts (~ 2 mm) are disseminated into the matrix and small fan-shaped muscovite (~ 200 μm) occurs at quartz phenocrysts boundaries.
EE2	Granite	Erzengel/Sosa	
GG1	Granite	Gabe Gottes/Dönitzgrund	
GG3	Granite	Gabe Gottes/Dönitzgrund	This sample is similar to samples BO1, EE2, and GG1 but here no large ferroan poly-lithionite occur and only small fan-shaped muscovite crystals are visible.
JG1 and JG2	Phyllite	Jugel NW	Some muscovite-tourmaline-cassiterite assemblages occur in fractures in the quartz matrix. Chloritized biotite may occur in association with this assemblage in fractures.
RZ2	Granite	Roßzeche/nördlich Carlsfeld	The matrix is mainly composed of quartz and biotite. Ferroan poly-lithionite phenocrysts occur disseminated in the matrix and small fan-shaped muscovite are visible at quartz phenocrysts boundaries.

respectively) that show two generations. In these samples, the first generation of ferroan poly-lithionite forms large white mica crystals (1–3 cm), whereas the second generation of muscovite forms small fan-shaped aggregates. In skarn samples, there is only one generation of mica. We characterized mica for the various greisen, metasomatized phyllites, and skarn samples by EPMA (Table 2 and Appendix 1). We use the classification of Tischendorf et al. (2001), which is based on the substitution of Li and Al for Mg and Fe, respectively, to group white mica from the various greisen and skarn samples (Fig. 6). The majority of samples plot in the compositional fields of (ferroan) muscovite and ferroan poly-lithionite. However, there are several distinct differences between first and second generation mica. For the Backofen greisen (BO1), first generation white mica shows a ferroan poly-lithionite composition, whereas second generation mica falls mainly in the field of muscovite and ferroan muscovite. At the Erzengel location (EE1), first generation greisen mica has mainly a ferroan poly-lithionite composition. The second generation shows a muscovite composition. In Gabe Gottes greisen (GG1), first generation mica shows a compositional range extending from ferroan poly-lithionite to lithian siderophyllite, whereas the second generation shows a muscovite composition with some Fe-rich crystals that plot in the ferroan muscovite field (Fig. 6). This classification highlights the occurrence of two generations of mica in the greisen sample GG3 from Gabe Gottes, in the metasomatized phyllite sample JG1 from Jugel, and in the amphibole skarn (HAS3) of

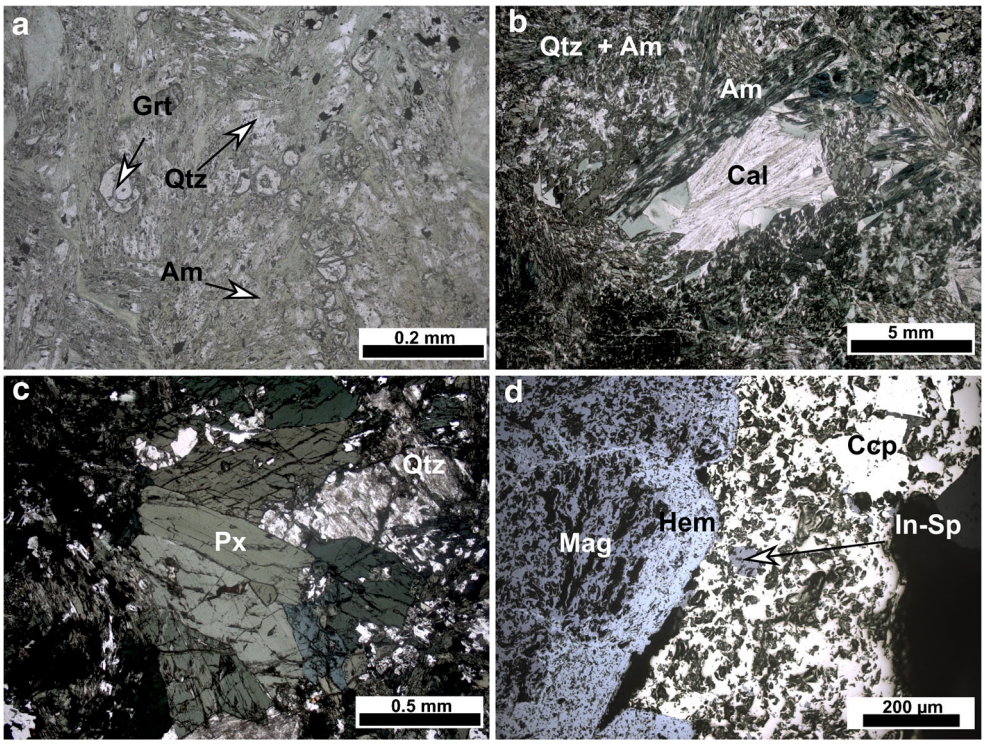

Fig. 4 Thin sections showing the typical mineral assemblages of the various skarn types. **a** Contact between garnet and amphibole skarns (sample HAS2) with garnet disseminated into the amphibole skarn mainly composed of amphibole and quartz. **b** Amphibole skarn (sample HAS1) with calcite surrounded by amphibole in a quartz-amphibole assemblage. **c** Pyroxene skarn (sample HPS1) with a pyroxene-quartz assemblage. **d** Magnetite skarn (sample HMS1) in reflected light showing a cluster of chalcopyrite in the magnetite-hematite assemblage. Indium-rich sphalerite occurs as inclusions in chalcopyrite. Am: amphibole, Cal: calcite, Ccp: chalcopyrite, Grt: garnet, Hem: hematite, In-Sp: In-sphalerite, Mag: magnetite, Px: pyroxene, Qtz: quartz

Hämmerlein. One generation shows a ferroan poly-lithionite composition, which can be close to zinnwaldite for Gabe Gottes and Jugel. The other generation has a muscovite composition in Gabe Gottes and Jugel, whereas it shows a ferroan muscovite composition in the amphibole skarn of Hämmerlein. The only generation of mica occurring in pyroxene skarn (CSV1) of Hämmerlein shows a ferroan muscovite composition. Figure 7 highlights the compositional contrast between the two generations of greisen mica in terms of major and trace elements. In greisen samples, first-generation white mica contains less Al than the second generation (~ 20 wt% vs. ~ 34 wt%). In contrast, Mg and Li contents of first generation white mica are higher than those of second generation white mica (~ 0.9-wt% vs. ~ 0.2-wt% Mg and ~ 2.2-apfu vs. 0.2-apfu Li). Fluorine is higher in the first generation greisen white mica, whereas Na content is higher in the second generation greisen white mica (Fig. 7). Tin is present in most greisen white mica samples with ~ 0.03-wt% Sn in first generation white mica and up to 0.13-wt% Sn in second generation white mica. Note, Sn contents in skarn white mica are below the detection limit of the electron microprobe (Table 2).

Compositional data of silicate minerals that are typical for the calc-silicate skarns and that are part of the prograde assemblage (garnet, amphibole, and pyroxene) is shown in Table 3. Garnet shows different compositions depending on the lithology where it is present. Ca-rich almandine occurs in massive garnet skarn (e.g., sample HGS1), whereas Fe-rich grossular has been found at contacts between garnet and amphibole skarns (e.g., sample HAS2). It is noticeable that grossular contains up to ~ 0.12-wt% Sn, whereas the Sn concentration in almandine is below the detection limit of the electron microprobe. Fe-rich cummingtonite in the amphibole skarn has up to ~ 0.07-wt% Sn, and Fe-rich augite in the pyroxene skarn shows up to ~ 0.45-wt% Sn.

Tourmaline crystals are common in greisen but occur also in some skarn samples. Greisen tourmaline is schorl whereas skarn tourmaline is foitite (Table 4). The main compositional difference between greisen and skarn tourmaline is the content of Na and, thus, the occupancy of the X-site. Schorl belongs to the alkali group of tourmaline, whereas foitite belongs to the X-site vacancy group (Hawthorne and Dirlam 2011) (Fig. 8). It is also noticeable that, in both kinds of tourmaline, Sn concentrations are below the detection limit of microprobe analysis.

Theriak-Domino modeling

The skarn type changes on the meter scale and locally even on the centimeter scale (Lefebvre et al. 2017). The sequence of skarn type is very variable on the scale of the mine. The close spatial coexistence of the different skarn types implies that they formed together under similar pressure and temperature conditions. The various calc-silicate skarn types of Hämmerlein have similar whole rock compositions (Appendix 2). Therefore, the contrasting mineralogical composition of the skarns reflects the presence of contrasting fluids and/or reactions. The fluid composition may be locally controlled by the consumption of carbonates that generates

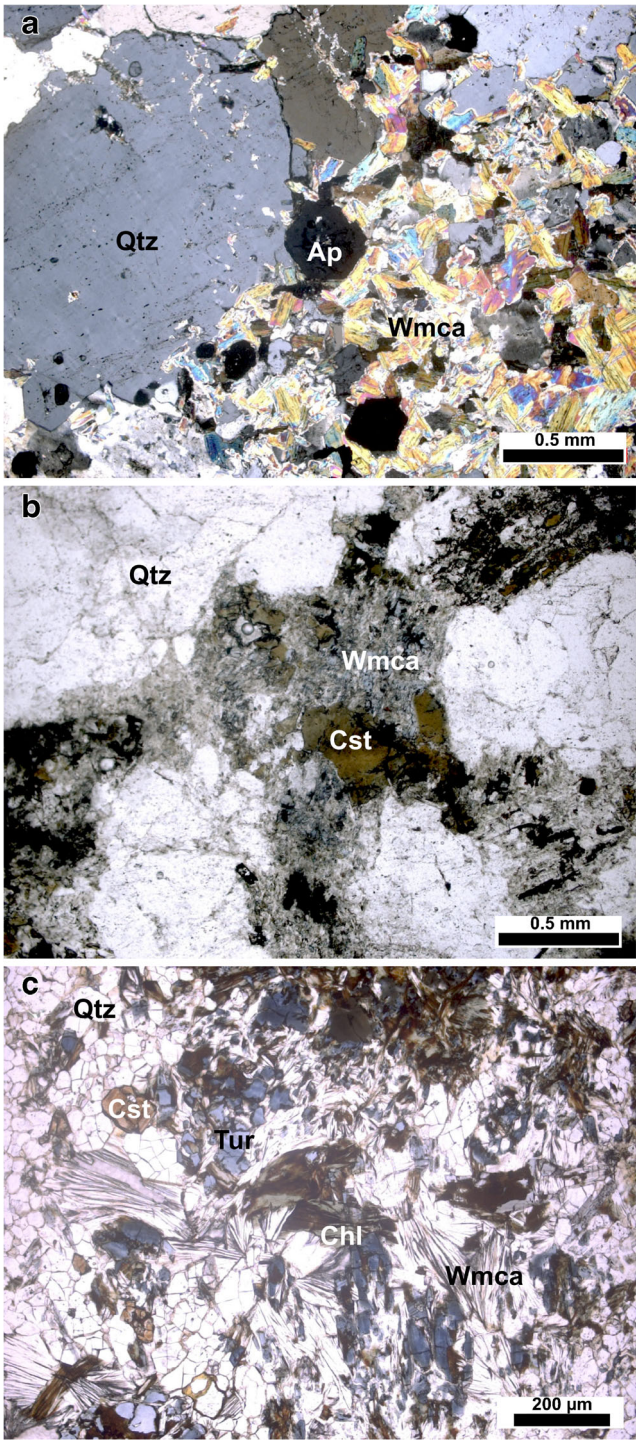

Fig. 5 Typical greisen mineral assemblages. **a** White mica-apatite assemblage embedded in the quartz (sample EE2). **b** White mica-cassiterite assemblage in the quartz (sample GG3). **c** White mica-chlorite-tourmaline-cassiterite assemblage (sample JG2). Ap: apatite, Chl: chlorite, Cst: cassiterite, Qtz: quartz, Tur: tourmaline, Wmca: white mica

CO_2, which may increase XCO_2 of the fluid or induce phase separation (Diamond 2001). The mineral assemblages of the skarns have been modeled (Fig. 9) in terms of temperature and XCO_2 at 2 and 5 kbar, respectively, using the Theriak-Domino thermodynamic modeling software of deCapitani and Petrakakis (2010). The compositions used for the modeling are the average skarn composition (see Appendix 2) for the silicate skarns and the composition of an individual sample for the magnetite skarn. The pressure of 2 kbar roughly corresponds to the emplacement depth of the Eibenstock granite (Förster et al. 1999) and, therefore, the depth of the skarnified wall rocks at the time of the granite emplacement. Thus, a pressure of 2 kbar would correspond to a situation of contact metamorphism with skarn formation triggered by fluids and heat from the granite. The pressure of 5 kbar roughly corresponds to the metamorphic conditions reached by the host-rocks of the skarn during the Variscan orogeny at c. 340 Ma (Rötzler et al. 1998), i.e., clearly before the emplacement of the granite.

Figure 9 shows the stability fields of the various skarn types for 2 and 5 kbar, respectively. The various skarn mineral assemblages include biotite, rutile or titanite, and calcite. The various skarns differ by the nature of the main calc-silicate minerals, i.e., garnet, amphibole, and pyroxene. The magnetite skarn assemblage is dominated by magnetite with minor biotite, pyroxene, and titanite. The most distinctive differences of the various stability fields are the contrasting ranges of XCO_2. At 5 kbar (Fig. 9b), the stability fields of the various skarns are relatively large and overlap, the garnet skarn mineral assemblage is stable at high XCO_2, whereas the amphibole, pyroxene, and magnetite skarns are stable at systematically lower XCO_2. The various stability fields have an overlapping temperature range at 400–450 °C. At 2 kbar (Fig. 9a), the stability fields of the various skarns are narrower than at 5 kbar and extend to lower temperatures. Garnet and magnetite skarns have clearly contrasting temperature ranges. Amphibole and pyroxene skarns, compared to garnet skarn, have broader temperature ranges that overlap with those of garnet skarn.

Rb-Sr age determination

Three groups of Rb-Sr multimineral ages have been determined for the skarn and greisen samples (Fig. 10). The youngest age of ~ 290 Ma was obtained for the greisen sample GG1. The other six dated greisen samples yield ages around 320 Ma, whereas the two samples from the Hämmerlein skarn deposit yield ages around 340 Ma.

For the greisen sample GG1, three size fractions (250–180, 180–125, and 125–90 μm) of white mica, the whole rock fraction, and one apatite fraction were analyzed. Two mica fractions (250–180 and 180–125 μm) and apatite together define an isochron age of 294.8 ± 3.1 Ma ($n = 3$, MSWD = 3.0) with an initial $^{87}Sr/^{86}Sr$ at 0.714604 ± 0.000042 (Fig. 10, Table 5). The whole rock and one white mica fraction plot slightly above the regression line and, therefore, they are

Table 2 Representative electron microprobe analyses of muscovite from greisen mineralizations spatially associated with the Eibenstock granite and from skarns from Hämmerlein

	Greisen and metasomatized phyllites										Skarn/gneiss	
	BO1 1st gen.	BO1 2nd gen.	EE2 1st gen.	EE2 2nd gen.	GG1 1st gen.	GG1 2nd gen.	GG3 1st gen.	GG3 2nd gen.	JG1	JG2	CSV1	HAS3
SiO_2	47.65	47.58	45.80	47.10	45.84	46.83	46.77	46.85	46.70	46.33	48.79	48.41
TiO_2	0.28	0.07	0.20	0.03	0.17	0.04	0.09	0.04	0.07	0.01	0.29	0.34
Al_2O_3	24.85	32.24	21.05	33.22	28.36	31.29	32.12	34.32	30.74	33.52	26.42	25.83
FeO	8.93	3.87	12.53	3.19	7.52	5.22	4.52	2.48	4.18	3.53	6.67	7.97
MgO	0.37	0.06	0.87	0.16	0.57	0.18	0.18	0.09	1.44	0.36	0.42	0.36
CaO	0.04	0.02	bdl	0.02	bdl	0.06	0.02	0.10	bdl	0.04	0.02	0.03
K_2O	10.17	10.56	10.17	10.62	10.58	10.17	10.79	10.47	10.61	10.55	10.40	10.30
Na_2O	0.07	0.15	0.10	0.14	0.08	0.18	0.22	0.27	0.28	0.27	0.12	0.11
MnO	0.16	0.08	0.22	0.09	0.16	0.04	0.05	0.05	0.01	0.03	0.18	0.21
BaO	0.06	0.07	0.12	0.03	0.11	0.15	0.04	0.08	0.07	0.14	0.11	0.07
P_2O_5	0.02	0.06	bdl	0.01	bdl	bdl	0.06	0.05	bdl	0.01	0.01	bdl
SnO_2	0.03	0.13	bdl	0.08	0.03	0.04	0.03	0.08	0.15	0.11	bdl	bdl
Li_2O	4.11	0.63	3.58	0.70	3.59	0.44	3.86	0.55	3.84	0.20	0.22	4.31
Cl	0.01	0.01	0.01	0.01	0.01	bdl	bdl	0.01	bdl	0.02	bdl	bdl
F	4.99	1.42	8.22	1.55	1.78	1.09	1.80	1.29	1.80	0.60	0.65	1.25
H_2O	bdl	3.78	0.26	3.73	0.32	3.87	0.21	3.87	0.19	4.15	4.00	3.71
Total	101.74	100.73	102.87	100.68	99.12	99.60	100.76	100.60	100.08	99.87	98.30	98.90
Si	6.4	6.4	6.5	6.3	6.2	6.4	6.1	6.2	6.1	6.3	6.8	6.4
Al (T)	1.6	1.6	1.5	1.7	1.8	1.6	1.9	1.7	1.9	1.7	1.2	1.6
K	1.7	1.8	1.8	1.8	1.8	1.8	1.8	1.8	1.8	1.8	1.8	1.7
Na	bdl	bdl	bdl	bdl	bdl	bdl	0.1	0.1	0.1	0.1	bdl	bdl
Al (M)	2.4	3.5	2.0	3.5	2.7	3.4	3.0	3.6	2.8	3.6	3.1	2.5
Fe	1.0	0.4	1.5	0.4	0.8	0.6	0.5	0.3	0.5	0.4	0.8	0.9
Mg	0.1	bdl	0.2	bdl	0.1	bdl	bdl	bdl	0.3	0.1	0.1	0.1
Li	2.2	0.3	2.0	0.4	1.9	0.2	2.0	0.3	2.0	0.1	0.1	2.3
F	2.1	0.6	3.7	0.7	0.8	0.5	0.7	0.5	0.7	0.3	0.3	0.5

Li_2O calculated after Tischendorf et al. (1997). Analytical data in wt%; mineral formula calculation results are given in apfu. Bdl: below detection limit. Additional analyses are given in the electronic supplement

excluded from the calculation. Note, using all samples to constrain calculate isochron parameters does not affect the age significantly, but increases considerably the uncertainty of age and of the initial Sr isotopic composition (Fig. 10).

The six other samples of greisen consistently yield Rb-Sr multimineral ages around 320 Ma (Fig. 10, Table 5). Greisen sample BO1 yields an isochron age of 319 ± 2.7 Ma ($n = 6$, MSWD = 2.2) with initial $^{87}Sr/^{86}Sr$ of 0.7044 ± 0.0063. The isochron is defined by three muscovite fractions (250–180, 180–125, and 125–90 μm) and one fraction each of white apatite, K-feldspar, and albite. Yellow apatite was not included in the regression. Its inclusion would not significantly affect the age information, but only deteriorate precision (see Fig. 10 for greisen sample EE2).

For greisen sample EE2, two muscovite (125–90 and 90–63 μm) and two apatite (yellow and white) fractions define an isochron with an age of 322.2 ± 3.3 Ma ($n = 4$, MSWD = 1.17) and an initial $^{87}Sr/^{86}Sr$ of 0.8587 ± 0.0029. Note, this initial Sr isotopic composition is significantly higher than initial $^{87}Sr/^{86}Sr$ for different types of Eibenstock granite (up to 0.713; Velichkin et al. 1994). Albite and K-feldspar have been omitted from the calculation of the isochron, as they plot below the isochron and would shift the apparent initial Sr isotopic composition to an unreasonably low value of 0.642 ± 0.052 (Fig. 10). We hypothesize that this effect is caused by crystallizational overprint of feldspar, potentially, by upper crustal fluids or by weathering.

The Rb-Sr age of sample GG3 is determined by an isochron constrained by four muscovite fractions (500–355, 355–250, 180–125, and 125–90 μm), two apatite fractions (yellow and white apatite), and one K-feldspar fraction, to be 319.8 ± 4.4 Ma ($n = 7$, MSWD = 7.5) with a poorly

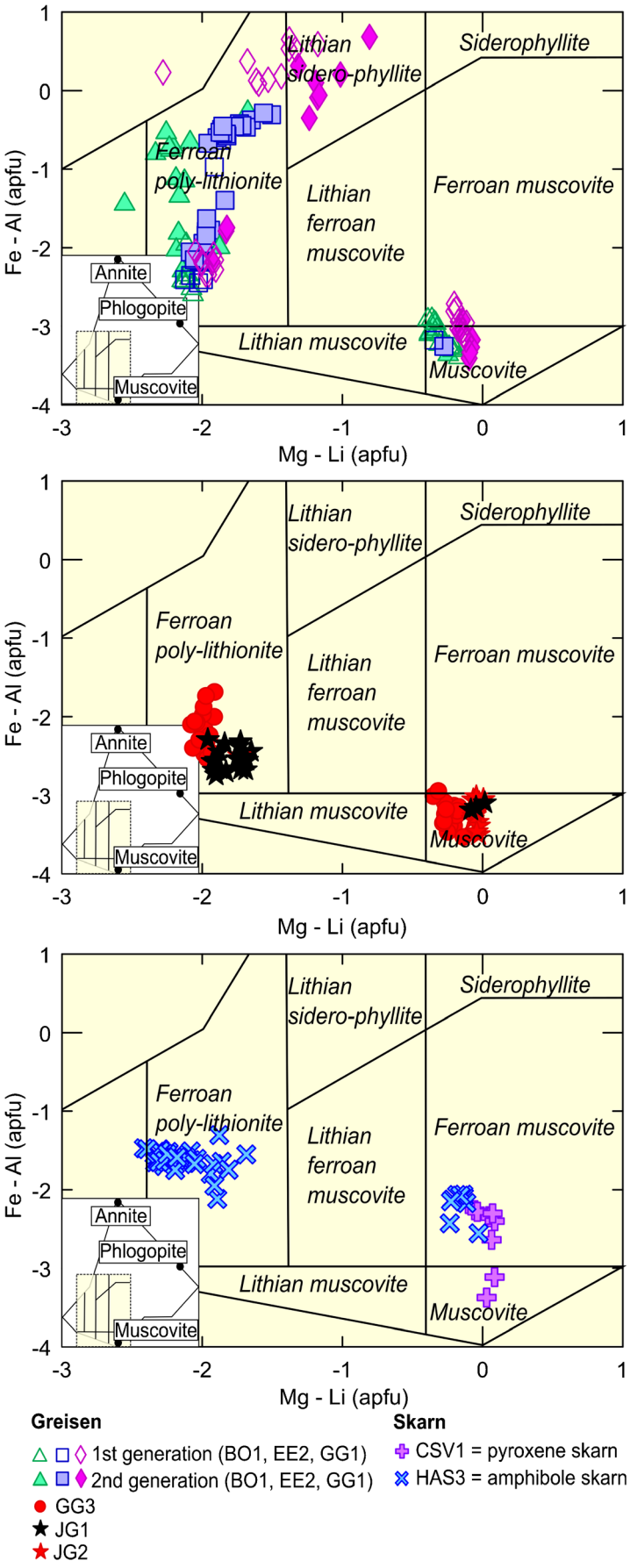

Fig. 6 Composition of white mica from the Hämmerlein skarn (**a**) and greisen mineralization associated with the Eibenstock granite (Backofen BO1, Erzengel EE2, and Gabe Gottes GG1 with two populations of micas (**b**) and Gabe Gottes GG3 and Jügel JG1/JG2 with one population (**c**)) in terms of FeAl vs MgLi (FeAl = $Fe_{tot} + Mn + Ti - Al^{VI}$; MgLi = Mg − Li in apfu). Data source: see Appendix 1. The insert represents the entire classification diagram (diagram modified from Tischendorf et al. 2001)

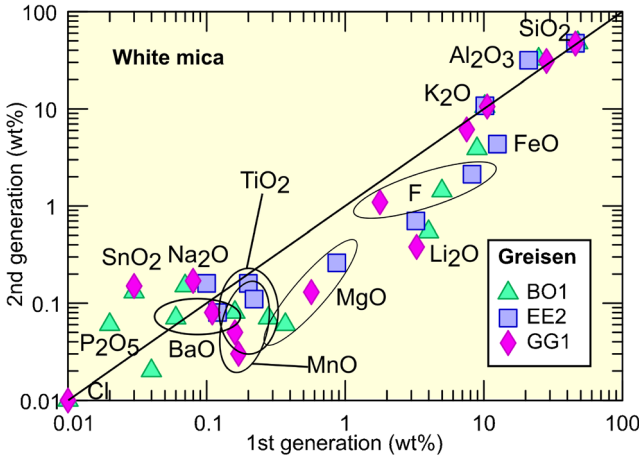

Fig. 7 Comparison of average major and trace elements content of the two generations of white mica from Backofen (BO1), Erzengel (EE2), and Gabe Gottes (GG1) greisen samples. The first generation contains more Fe, Mg, Mn, Ti, Li, and F, whereas the second generation is enriched in Na, P, and Sn

constrained initial $^{87}Sr/^{86}Sr$ ratio of 0.71 ± 0.16 (Fig. 10). The excess scatter (indicated by the elevated MSWD) cannot be assigned to one particular mineral fraction. In any case, the large range in $^{87}Rb/^{86}Sr$ values spanned by the four white mica samples renders the slope of the isochron nearly insensitive to potential secondary alterations of the low-$^{87}Rb/^{86}Sr$ mineral fractions.

Metasomatized phyllite sample JG1 is unusual among the here dated greisen samples as it has the smallest range in $^{87}Sr/^{86}Sr$ with a maximum $^{87}Sr/^{86}Sr$ as low as 1.04240 (Table 5). The slope of the isochron is constrained by three grain size fractions of muscovite (500–355, 180–125, and 125–90 μm) and one tourmaline fraction. The isochron yields an age of 322.1 ± 2.8 Ma (n = 4, MSWD = 2.7) with an initial $^{87}Sr/^{86}Sr$ of 0.72125 ± 0.00018 (Fig. 10). A second sample from the same metasomatized phyllite, sample JG2, yields a five-point isochron that is defined by three muscovite fractions (355–250, 125–90, and 90–63 μm) and two tourmaline fractions (355–250 and 250–180 μm). The isochron corresponds to an age of 317.7 ± 3.0 Ma (n = 5, MSWD = 1.7) and yields an initial $^{87}Sr/^{86}Sr$ of 0.72169 ± 0.00048 (Fig. 10). The ages and initial $^{87}Sr/^{86}Sr$ values of these two greisen samples overlap within respective uncertainties.

Greisen sample RZ2 shows significant scatter among low-$^{87}Sr/^{86}Sr$ phases (albite, apatite, K-feldspar). Furthermore, the coarser white mica fraction does not fall on the same regression line as the other fractions. Instead, the 2–5-mm white mica fraction plots above this regression line, implying that the coarsest mica did not re-equilibrate during later recrystallization events that partially or completely reset the finer mica fractions. The age of 311.9 ± 6.8 Ma (n = 5, MSWD = 14) and the initial $^{87}Sr/^{86}Sr$ of 0.75 ± 0.12 (Fig. 10) were obtained from isochronal regression fitted to three white mica fractions (355–250, 180–125, and 125–90 μm), one apatite fraction, and one K-feldspar fraction. It is unclear whether this regression line is geologically meaningful or only constitutes a rotated mixing line. The coarse-grained white mica fraction (5–2 mm) and the albite fraction, which plot below the regression line defined by the other fractions, yield a two-point line corresponding to an age of 326.2 ± 4.8 Ma with an initial $^{87}Sr/^{86}Sr$ of 0.716309 ± 0.000042 (Fig. 10). Although the crystallization age of the RZ2 greisen sample is not well constrained, the values of

Table 3 Representative electron microprobe analyses of garnet, amphibole, and pyroxene from skarns from Hämmerlein

	HAS2 Grt	HGS1 Grt	HAS2 Am	CSV1 Px
SiO_2	38.08	37.64	29.47	38.61
TiO_2	0.06	0.11	0.02	0.09
Al_2O_3	16.94	20.90	15.28	10.31
FeO	10.55	27.82	20.25	32.36
MgO	0.21	1.17	19.04	1.08
CaO	28.55	9.71	0.08	10.98
K_2O	0.02	bdl	0.04	1.70
Na_2O	bdl	0.03	0.01	1.16
Cr_2O_3	bdl	0.02	0.02	bdl
MnO	4.54	1.99	2.22	0.73
SnO_2	0.12	bdl	0.07	0.45
Total	99.07	99.40	86.50	97.47
Si	3	3	4.8	1.6
Al iv	–	–	2.9	0.4
Fe^{3+}	–	–	2.6	–
Fe^{2+}	0.3	1.9	bdl	0.4
Mn	0.3	0.1	bdl	bdl
Mg	bdl	0.1	bdl	bdl
Ca	2.4	0.8	bdl	0.5
Na	–	–	–	0.1
Total	3.0	2.9	2.6	1.0
Mg	–	–	4.6	bdl
Mn	–	–	0.3	–
Ti	bdl	bdl	bdl	bdl
Al	1.6	2.0	bdl	0.2
Cr	bdl	bdl	bdl	bdl
Fe^{3+}	0.4	bdl	0.1	0.3
Fe^{2+}	–	–	–	0.5
Total	2.0	2.0	5.0	1.0
Classified as	Grs	Alm	Cum	Aug

Fe^{2+} and Fe^{3+} calculated after Brady and Perkins (2015) for garnet and pyroxene, after Leake et al. (1997) for amphibole. Analytical data in wt%; mineral formula calculation results are given in apfu. Bdl: below detection limit. Alm: almandine, Am; amphibole, Aug: augite, Cum: cummingtonite, Grs: grossular, Grt: garnet, Px: pyroxene. Additional analyses are given in the electronic supplement

Table 4 Representative electron microprobe analyses of tourmalines from greisen and skarns from Hämmerlein

	Greisen			Skarn
	GG3	JG1	JG2	HAS1
B_2O_3	10.26	10.34	10.32	9.34
SiO_2	34.39	35.70	35.40	27.99
TiO_2	0.63	0.09	0.01	0.04
Al_2O_3	32.17	29.74	31.53	19.44
FeO	17.16	15.88	17.79	28.58
MgO	0.55	3.57	0.86	11.24
CaO	0.07	0.81	0.44	0.09
K_2O	0.07	0.03	0.03	0.51
Na_2O	2.42	2.16	2.09	0.03
BaO	0.08	0.08	0.08	0.07
MnO	0.17	0.06	0.06	0.13
Cl	bdl	0.01	0.01	0.01
F	1.14	0.30	0.44	bdl
Li_2O	0.12	bdl	0.07	bdl
H_2O	3.00	3.42	3.35	3.22
Total	102.23	102.19	102.48	100.69
B	3	3	3	3
Si	5.83	6	5.96	5.21
Al (T)	0.17	bdl	0.04	0.79
Al (Z)	6	5.89	6	3.47
Mg (Z)	bdl	0.11	bdl	2.53
Fe^{2+}	2.43	2.23	2.51	2.45
Ti	0.08	0.01	bdl	0.01
Al (Y)	0.25	bdl	0.22	bdl
Mn	0.02	0.01	0.01	0.02
Mg	0.14	0.78	0.22	0.65
Li	0.08	bdl	0.05	bdl
Total Y	3	3.03	3	3.13
Na	0.80	0.70	0.68	0.01
Ca	0.01	0.15	0.08	0.02
[]	0.17	0.14	0.23	0.85
K	0.02	0.01	0.01	0.12
Total X	1	1	1	1
OH (V)	3	3	3	3
OH (W)	0.39	0.84	0.76	1
F (W)	0.61	0.16	0.23	bdl
Classified as	Schorl	Schorl	Schorl	Foitite

B_2O_3, Li_2O and H_2O calculated after Selway and Xiong (2015). Analytical data in wt%; mineral formula calculation results are given in apfu. Bdl: below detection limit. Additional analyses are given in the electronic supplement

311.9 ± 6.8 and 326.2 ± 4.8 Ma are likely to bracket the age of greisen formation.

Two gneiss samples with skarn have been dated (Fig. 10, Table 5). Sample CSV1 yields an age of 341.2 ± 3.8 Ma ($n = 6$, MSWD = 325) with an initial $^{87}Sr/^{86}Sr$ of 0.7241 ± 0.0082 (Fig. 10). The calculation is based on four white mica grain size fractions (500–355, 355–250, 180–125, and 125–90 μm), one K-feldspar fraction, and one epidote fraction. The albite and fluorite fractions plot considerably above the regression line and, therefore, have not been included into the calculation. The fluorite fraction has a low $^{87}Rb/^{86}Sr$ of 0.0529 and, therefore, its radiogenic $^{87}Sr/^{86}Sr$ (1.0561) (Fig. 10, Table 5) implies that this texturally late fluorite crystallized from a fluid with higher $^{87}Sr/^{86}Sr$ than the fluid that formed the skarn silicates used for isotopic dating.

The Rb-Sr age of the sample HAS3 was determined using four muscovite fractions (500–355, 355–250, 180–125, and 125–90 μm), K-feldspar, and purple fluorite. Regression yields an age of 337.0 ± 3.9 Ma ($n = 6$, MSWD = 59) with an initial $^{87}Sr/^{86}Sr$ of 0.729 ± 0.027 (Fig. 10). The blue fluorite plots far above the regression line and was not used to calculate the age. The abnormally high Sr isotopic signature of this fluorite requires, as in sample CSV1, post-crystallizational influx of high-$^{87}Sr/^{86}Sr$ fluorite precipitating fluids. The high strain-induced layering and the metamorphism of both the gneiss and the skarn are related to the same ductile event (Fig. 3). Therefore, the age obtained for white mica, which likely belong to the gneiss, also yields the age of the skarn.

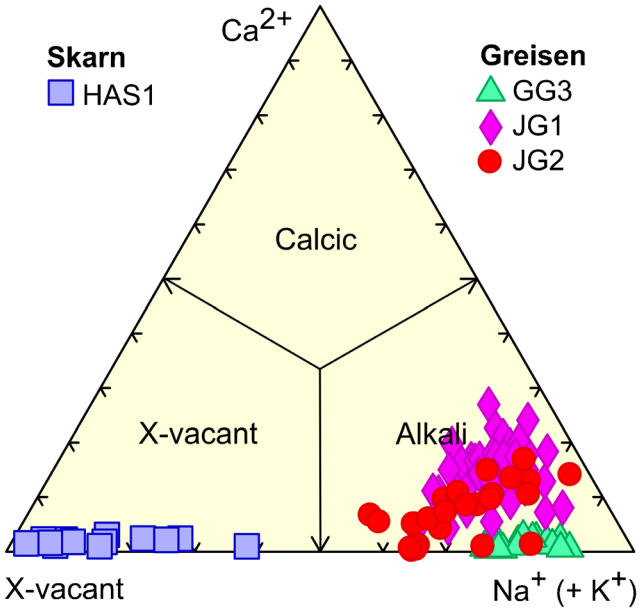

Fig. 8 Classification diagram for tourmaline based on the occupancy of the X site. Tourmaline from greisen samples GG3, JG1, and JG2 is part of the alkali group, whereas tourmaline from the skarn HAS1 is distinctive by very low Ca-occupancy. This tourmaline falls in the field of X-vacant tourmaline and defines a broad range from the X-vacant compositions toward variable X-occupancy by Na and K (diagram modified after Hawthorne and Dirlam 2011)

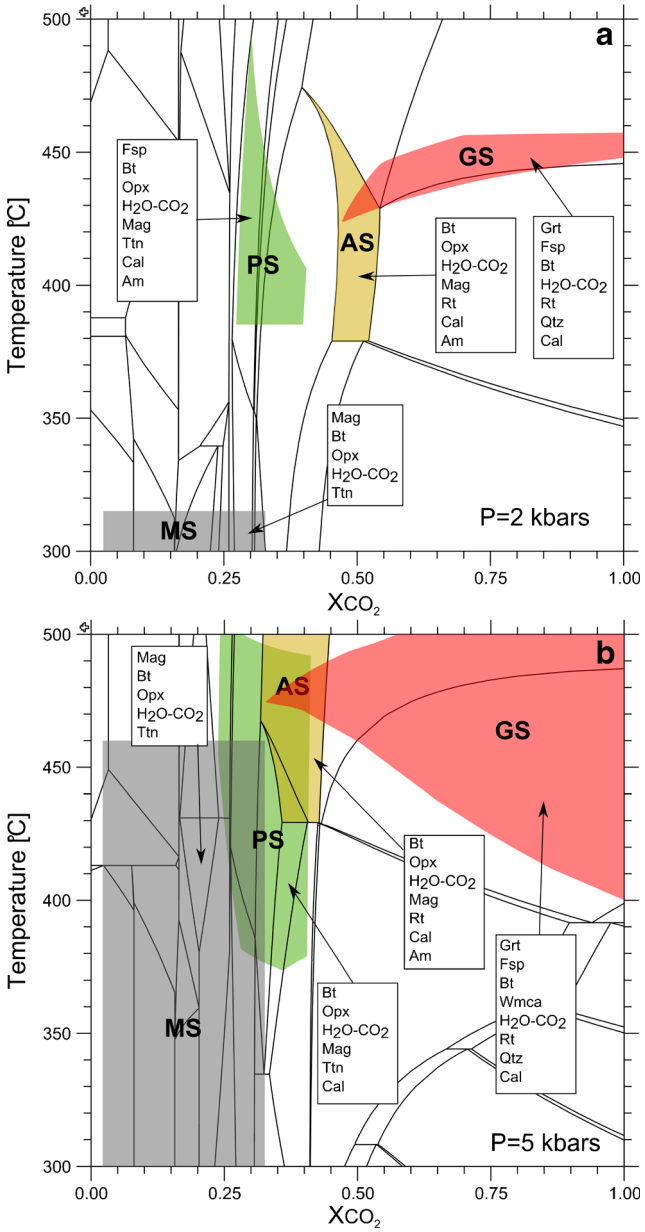

Fig. 9 Simplified T-P-XCO_2 modeling of the stability ranges of the various skarn assemblages at 2 kbar (**a**) and 5 kbar (**b**), respectively. Independent of pressure, the major difference among the various skarn assemblages is XCO_2, which increases systematically from magnetite skarn to pyroxene, amphibole, and garnet skarn. For 5 kbar, the various skarn types are stable in the same temperature range, whereas at 2 kbar, the magnetite skarn is stable at lower temperature. Individual modeling parameters for each skarn unit are available in the Appendices 2 and 3. Am: amphibole, Bt: biotite, Cal: calcite, Fsp: feldspar, Grt: garnet, Mag: magnetite, Opx: orthopyroxene, Qtz: quartz, Rt: rutile, Ttn: titanite, Wmca: white mica

Pb isotopic composition of skarn minerals of the Hämmerlein deposit

The Pb isotopic compositions of skarn silicates and sulfides are listed in Table 6 and plotted in Fig. 11. The data fall into two groups: one group includes samples with relatively unradiogenic Pb isotopic composition ($^{206}Pb/^{204}Pb_{meas}$, 18.36–19.1) and the other group has relatively radiogenic Pb isotopic composition ($^{206}Pb/^{204}Pb_{meas}$, 20.9–33.2). The difference between the two groups that do not form a continuous trend is most obvious in the $^{206}Pb/^{204}Pb$ vs. $^{238}U/^{204}Pb$ diagram (Fig. 11b). Minerals that formed during the regional Variscan metamorphism, maintained a closed U-Pb system, and had similar initial Pb isotopic compositions should fall on a straight line whose slope corresponds to an age of 340 Ma and whose intercept corresponds to the common initial Pb isotopic composition. All mineral samples of the first group fall on such a line, whereas all samples of the second group plot above this line (Fig. 11b). Minerals of the first group are derived from the garnet, pyroxene, and magnetite skarns and include garnet, sulfides, feldspar, and amphibole. There are also two amphibole and three apatite samples from the amphibole skarn that plot on this trend. Most minerals of this low-$^{206}Pb/^{204}Pb$ group form a tight cluster in the $^{206}Pb/^{204}Pb$-$^{207}Pb/^{204}Pb$ and $^{206}Pb/^{204}Pb$-$^{208}Pb/^{204}Pb$ diagrams (Fig. 11a, c).

Minerals of the second high-$^{206}Pb/^{204}Pb$ group all come from the amphibole skarn and include one amphibole and three apatite samples (Fig. 11). Initial $^{206}Pb/^{204}Pb$ values calculated for the ages of 340 and 320 Ma, respectively, are very radiogenic for these minerals. Furthermore, the various samples have different calculated initial $^{206}Pb/^{204}Pb$ values (Fig. 11b). In the $^{206}Pb/^{204}Pb$-$^{207}Pb/^{204}Pb$ diagram (Fig. 11a), these samples also show high $^{207}Pb/^{204}Pb$, which implies that their Pb either comes from a different source or has a poly-stage development. Such a poly-stage development also is indicated by the Sr isotopic composition of fluorite and apatite form amphibole skarn that have anomalously radiogenic initial $^{87}Sr/^{86}Sr$ values and fall far above the Rb-Sr isochron. For a simple two-stage Pb-growth for skarn formation during regional metamorphism at 340 Ma and disturbance during emplacement of the Eibenstock granite at c. 320 Ma, the offset in the $^{206}Pb/^{204}Pb$ vs. $^{238}U/^{204}Pb$ diagram and the scatter in the $^{206}Pb/^{204}Pb$-$^{207}Pb/^{204}Pb$ and $^{206}Pb/^{204}Pb$-$^{208}Pb/^{204}Pb$ diagrams is best explained by Pb growth from 340 to 320 Ma with a high μ ($^{238}U/^{204}Pb$), followed by Pb growth from 320 Ma to present with a lower-μ value. Note, the age of c. 340 Ma is implied by the Rb-Sr isochron obtained for minerals from the same sample. In contrast, the age of c. 320 Ma is not closely constrained by the data. The various minerals that fall on the trend with the low initial $^{206}Pb/^{204}Pb$ in the $^{206}Pb/^{204}Pb$ vs. $^{238}U/^{204}Pb$ diagram did not see such a high-μ stage. Instead, these samples always had a low μ (even in case they had seen the same two-stage development). There are two possible scenarios for such a two-stage Pb growth: (i) In a first stage that lasted from 340 to c. 320 Ma, apatite and

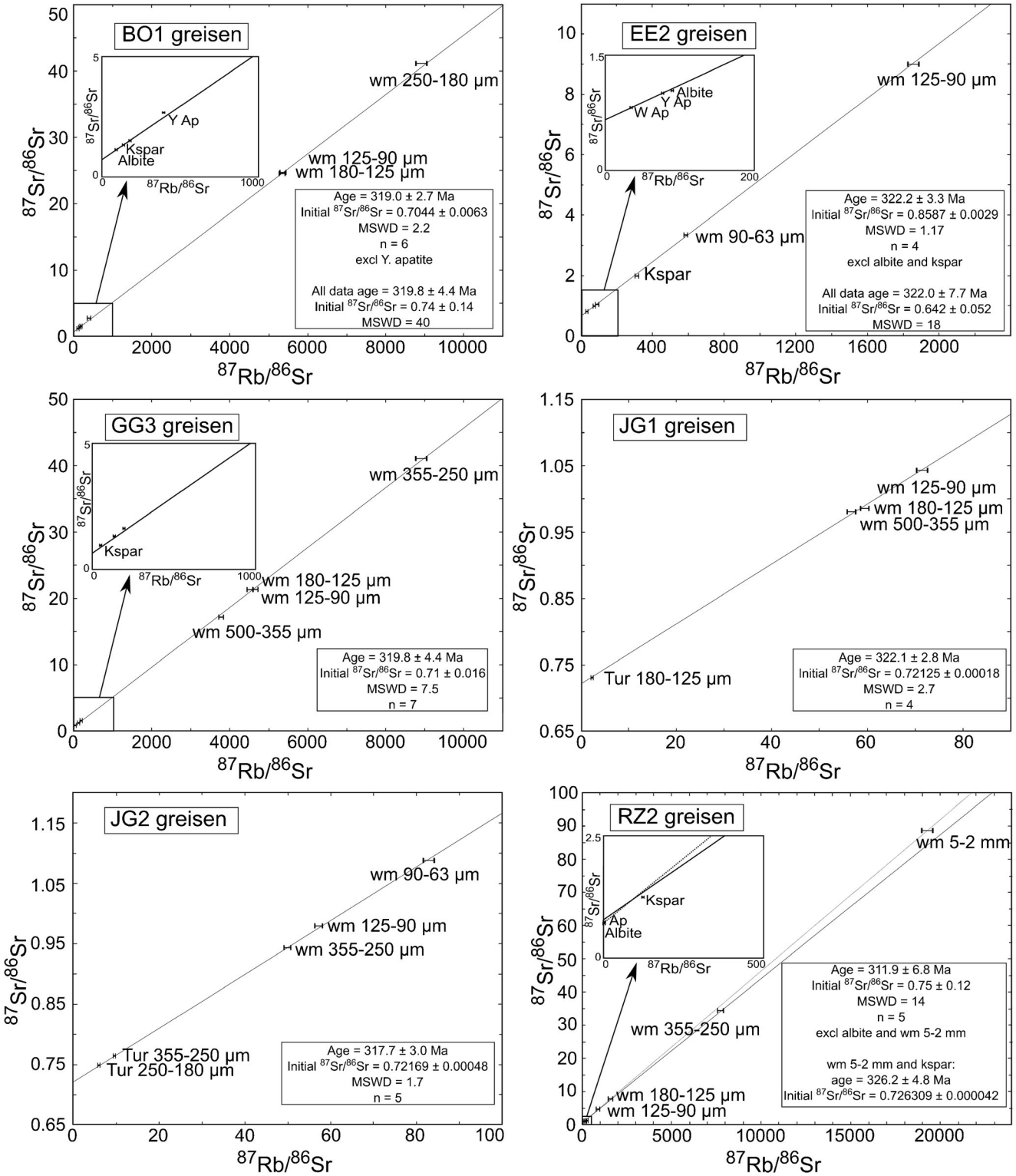

Fig. 10 Rb-Sr mineral data for greisen mineralization associated with the Eibenstock granite and skarns from Hämmerlein. Analytical data: see Table 4. Ap: apatite, Kspar: K-feldspar, Tur: tourmaline, W Ap: white apatite, Wm: white mica, Y Ap: yellow apatite

amphibole would have high $^{238}U/^{204}Pb$ and, thus, develop markedly higher $^{206}Pb/^{204}Pb$ and $^{207}Pb/^{204}Pb$ values that the other skarn minerals. During a second event at c. 320 Ma, apatite and amphibole would lose U (and Th). (ii) Apatite formed at c. 320 Ma and incorporated Pb that was derived from a source that had evolved in a high-μ environment. Such a late addition of radiogenic lead also would explain the restricted variation of $^{208}Pb/^{204}Pb$ at very

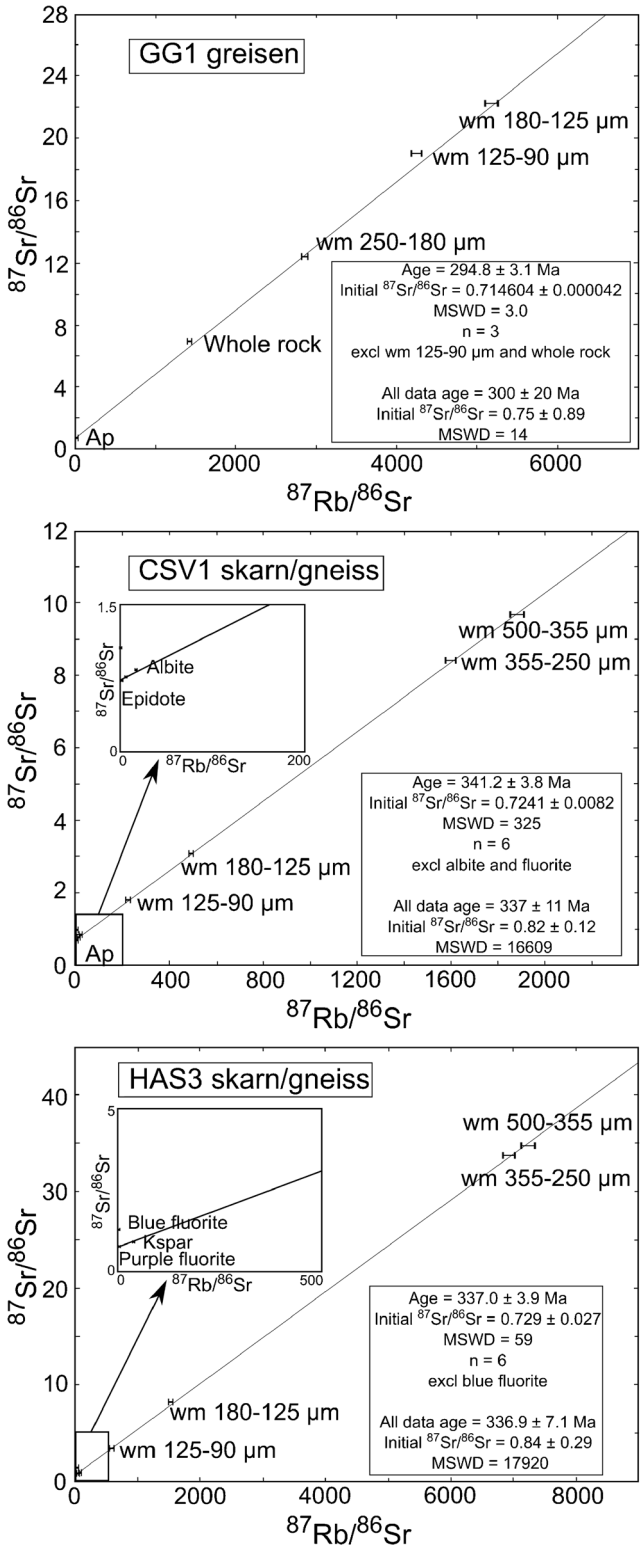

Fig. 10 (continued)

variable $^{206}Pb/^{204}Pb$, as Th is considerably less mobile in medium and low temperature fluids than U and Pb and, thus, was not available for incorporation (schematically indicated by the dashed trend lines for Th/U < 0.1 in Fig. 11c).

Discussion

Age of skarn formation

The Rb-Sr age determination on two gneiss samples with skarn (CSV1 and HAS3) yields ages at 341.2 ± 3.8 and 337.0 ± 3.9 Ma, respectively. The structural observations indicate that both the dated gneisses and the skarn in contact with the gneisses are pervasively foliated and thus reflect ductile conditions. As the metamorphic rocks of the Erzgebirge had cooled below the ductile-brittle transition long before 330 Ma, it is clear that the skarn formation is older than 330 Ma. Decarbonation is driven by the influx of aqueous fluids (e.g., Heinrich 2007). Aqueous fluids become available during prograde metamorphism by the dehydration of hydrous minerals rather than during post-peak cooling. Therefore, it is quite possible that the age of the skarn is close to the Rb-Sr age of the gneisses. Besides, simple thermodynamic modeling using Theriak-Domino and the whole rock composition of the various skarn types demonstrates that the stable mineral assemblages may be obtained at pressures of 5 kbar, which corresponds to peak conditions of regional metamorphism in the area at 340 Ma and is coherent with the Rb-Sr age of the skarn/gneiss. The prograde skarn assemblages formed at this time at ~ 5 kbar at ambient temperature of ~ 450 °C and contrasting XCO_2 (Fig. 9) corresponding to the four skarn types. However, the same minerals assemblages are also stable at lower pressure (Fig. 9a). This means that the skarn assemblages could not be destabilized at the pressure conditions prevailing during the emplacement of the Eibenstock granite (2 kbar) and that the calc-silicate assemblages may not be affected by major retrogression. Locally, strong chloritization as well as apatite formation affects the primary skarn assemblage. The age of this retrograde mineral assemblage is not known. It may represent retrogression after peak metamorphic conditions, retrogression caused by the Eibenstock granite intrusion, or retrogression related to even younger disturbances. The anomalously radiogenic Sr isotopic composition of apatite and fluorite and the Pb isotopic composition of apatite and amphibole, however, indicate that there must have elapsed a significant period of time after the formation of the skarn and its retrogression. Thus, chloritization with associated cassiterite and the formation of apatite and fluorite are not related to the 340-Ma metamorphism.

Age of greisen mineralization, age, and source of tin additions in greisen and skarn

Late stages of the Eibenstock and related granites (e.g., Kirchberg, Pobershau, Satzung) are major sources of Sn mineralization, as demonstrated by the abundance of Sn-rich greisen, some of which have been dated here (Table 5, Fig. 10). The dated greisen samples yield Rb-Sr isotopic ages ranging

Table 5 Rb/Sr analytical data of Hämmerlein skarns, and of greisen associated with the Eibenstock granite

Sample	Material	Rb (ppm)	Sr (ppm)	$^{87}Rb/^{86}Sr$	$^{87}Sr/^{86}Sr$	$^{87}Sr/^{86}Sr$ $2\sigma_m$ (%)
Skarn/gneiss samples						
CSV1 (Hämmerlein) (341.2 ± 3.8 Ma (excl. albite, apatite, and fluorite); MSWD = 325, Sr_i = 0.7241 ± 0.0082)						
MLP06	wm 500–355 μm	2094	6.04	1883	9.68243	0.0012
MLP07	wm 355–250 μm	2033	6.45	1599	8.41746	0.0018
MLP08	wm 180–125 μm	1990	14.3	494	3.07608	0.0010
MLP09	wm 125–90 μm	1834	26.4	222	1.78948	0.0011
MLP10	Fluorite	19.6	1109	0.0529	1.05602	0.0021
MLP11	Epidote	423	860	1.43	0.72624	0.0046
MLP12	Ap	114	2666	0.126	0.93551	0.0019
MLP13	Albite	206	35.4	17.1	0.83217	0.0014
MLP14	Kspar	410	195	6.11	0.75788	0.0010
HAS3 (Hämmerlein) (337.0 ± 3.9 Ma (excl. blue fluorite); MSWD = 59, Sr_i = 0.729 ± 0.027)						
MLP34	wm 500–355 μm	2014	3.50	7226	34.839	0.0040
MLP35	wm 355–250 μm	2024	3.57	6930	33.7152	0.0012
MLP36	wm 180–125 μm	1986	6.21	1609	8.25514	0.0006
MLP37	wm 125–90 μm	1780	11.3	578	3.45693	0.0008
MLP39	Kspar	1189	92.1	38.0	0.89841	0.0016
MLP40	Purple fluorite	81.5	125	1.89	0.75044	0.0061
MLP41	Blue fluorite	23.4	738	0.0969	1.27200	0.0036
Greisen samples						
BO1 (Backofen/Sosa) (319.0 ± 2.7 Ma (excl. Y. apatite); MSWD = 2.2, Sr_i = 0.7044 ± 0.0063)						
MLP57	wm 250–180 μm	3881	6.23	8905	40.9793	0.0020
MLP58	wm 180–125 μm	3852	6.94	5354	24.5610	0.0010
MLP59	wm 125–90 μm	3595	6.49	5336	24.5019	0.0009
MLP60	Albite	350	11.7	89.8	1.11015	0.0013
MLP61	Kspar	1082	24.2	137	1.31150	0.0028
MLP62	Y Ap	712	6.23	394	2.67194	0.0020
MLP63	W Ap	164	2.85	179	1.49377	0.0040
EE2 (Erzengel/Sosa) (322.2 ± 3.3 Ma (excl. albite and kspar); MSWD = 1.17, Sr_i = 0.6587 ± 0.0029)						
MLP16	wm 125–90 μm	3277	9.27	1851	8.9844	0.0040
MLP17	wm 90–63 μm	2698	16.7	587	3.32459	0.0014
MLP18	Kspar	827	8.66	311	1.98703	0.0012
MLP19	Albite	38.4	1.27	90.0	1.04228	0.0036
MLP65	Y Ap	370	14.3	76.9	1.00298	0.0020
MLP66	W Ap	72.5	6.13	34.5	0.81505	0.0040
GG1 (Gabe Gottes/Dönitzgrund) (294.8 ± 3.1 Ma (excl. wm 125–90 μm and whole rock); MSWD = 3.0, Sr_i = 0.714604 ± 0.000042)						
MLP01	wm 180–125 μm	2564	4.46	5176	22.2708	0.0019
MLP02	wm 250–180 μm	1799	3.91	2854	12.3836	0.0022
MLP03	wm 125–90 μm	2259	4.30	4248	19.0493	0.0020
MLP04	Ap	59.1	535	0.320	0.71592	0.0040
MLP64	whole rock > 500 μm	1082	3.52	1426	6.8970	0.0060
GG3 (Gabe Gottes/Dönitzgrund) (319.8 ± 4.4 Ma; MSWD = 7.5, Sr_i = 0.71 ± 0.16)						
MLP42	wm 500–355 μm	2487	5.02	3736	17.1464	0.0006
MLP43	wm 355–250 μm	2541	4.08	8917	41.0440	0.0012
MLP44	wm 180–125 μm	2560	4.85	4603	21.2957	0.0010
MLP45	wm 125–90 μm	2537	4.82	4589	21.2927	0.0022
MLP46	Kspar	968	56.0	51.2	0.95391	0.0011
MLP47	W Ap	151	3.44	134	1.3156	0.0077

Table 5 (continued)

Sample	Material	Rb (ppm)	Sr (ppm)	$^{87}Rb/^{86}Sr$	$^{87}Sr/^{86}Sr$	$^{87}Sr/^{86}Sr$ $2\sigma_m$ (%)
MLP48	Y Ap	1057	17.1	194	1.62713	0.0040
JG1 (Jugel NW) (322.1 ± 2.8 Ma; MSWD = 2.7, Sr_i = 0.72125 ± 0.00018)						
MLP22	wm 500–355 μm	1713	89.8	56.7	0.98019	0.0013
MLP23	wm 180–125 μm	1697	84.9	59.4	0.98621	0.0020
MLP24	wm 125–90 μm	1563	65.4	71.3	1.04240	0.0014
MLP27	Tur 180–125 μm	144	185	2.26	0.73147	0.0016
JG2 (Jugel NW) (317.7 ± 3.0 Ma; MSWD = 1.7, Sr_i = 0.72169 ± 0.00048)						
MLP28	wm 355–250 μm	1167	69.3	49.8	0.94236	0.0012
MLP30	wm 125–90 μm	1172	60.8	57.2	0.97975	0.0020
MLP31	wm 90–63 μm	1256	45.4	82.9	1.08731	0.0012
MLP32	Tur 355–250 μm	327	99.2	9.60	0.76441	0.0011
MLP33	Tur 250–180 μm	244	119	5.98	0.74830	0.0011
RZ2 (Roßzeche/nördlich Carlsfeld) (2311.9 ± 6.8 Ma (excl. wm 5–2 mm and albite); MSWD = 14, Sr_i = 0.75 ± 0.12)						
MLP49	wm 5–2 mm	4007	5.78	19,277	88.766	0.0020
MLP50	wm 355–250 μm	3919	6.28	7739	34.3233	0.0020
MLP51	wm 180–125 μm	3697	11.3	1604	7.7957	0.0020
MLP52	wm 125–90 μm	3533	15.8	900	4.74661	0.0005
MLP53	Albite	29.5	410	0.208	0.71726	0.0052
MLP54	Kspar	297	7.38	122	1.23730	0.0014
MLP55	Ap	16.0	597	0.0775	0.72510	0.0014

Ap: apatite, Kspar: K-feldspar, Tur: tourmaline, W Ap: white apatite, Wm: white mica, Y Ap: yellow apatite

from 322.2 ± 3.3 to 311.9 ± 6.8 Ma, which is essentially identical to the U-Pb zircon age range of the granite (314 ± 6 Ma, Tichomirowa et al. 2016). There is only one greisen sample that yields a distinctly younger age (294.8 ± 3.1 Ma, Fig. 10), which indicates that some of the greisen have been possibly overprinted during later events.

Cassiterite is the major Sn mineral in the greisen. It is texturally clearly related to the greisen formation and not to a later event. This is also corroborated by the enhanced Sn contents of greisen silicates. Typically, Sn contents of white mica range between 0.03 and 0.36 wt% (Appendix 1). This implies that late-magmatic fluids available at the time of emplacement of the Eibenstock and related granites transported Sn, and, therefore, Sn has been introduced into the greisen by fluids released from these granites. Furthermore, this also implies that these fluids may have introduced Sn into the skarn.

If all tin in the Hämmerlein skarn mineralization was derived from the Eibenstock granite, older skarn minerals should not have elevated Sn contents. Instead, only secondary skarn minerals that formed during the same event as secondary fluorite and chlorite should have elevated Sn contents. Primary 340-Ma old skarn minerals in the Hämmerlein deposit, however, do have elevated Sn contents. For instance, grossular from the garnet skarn has 0.10 to 0.88 wt% Sn (Appendix 1). Similarly, cummingtonite from the amphibole skarn has 0.03- to 0.49-wt% Sn, and augite from the pyroxene skarn has 0.45 to 0.77-wt% Sn (Appendix 1). This implies that Sn was available for incorporation at 340 Ma and must have been introduced into the skarn in the process of Variscan regional metamorphism, i.e., c. 20 Ma before the emplacement of the Eibenstock and related granites. During this early event of Sn mobilization, Sn did not form early stage cassiterite, but was incorporated into skarn minerals. The later alteration of some of these skarn minerals may have released Sn that was then precipitated as cassiterite. Such a formation of secondary ore minerals during the alteration of biotite to chlorite has been described by Zhao et al. (2005) and Wang et al. (2013). For the Hämmerlein skarn, the amount of chlorite is relatively small. Thus, the release of Sn during the consumption of biotite, or muscovite, or garnet to form chlorite seems insufficient to explain the observed amount of cassiterite. Thus, the Hämmerlein skarn experienced two phases of Sn accumulation: one during regional metamorphism and one during the emplacement of the Eibenstock and related granites. During the first event of Sn addition, the devolatilizing sedimentary rocks beneath the later skarn seem to represent the Sn source, whereas during the second event Sn was brought along by late magmatic fluids emanating from the Eibenstock granite and resulting in the superimposition of tin mineralization on the previous skarn, just in the same way as in the Huanggangliang Fe-Sn skarn in Inner Mongolia (Wang et al. 2001).

Table 6 U/Pb analytical data of Hämmerlein skarns

Sample no.	Material	U (ppm)	Pb (ppm)	$^{206}Pb/^{204}Pb$	$^{207}Pb/^{204}Pb$	$^{208}Pb/^{204}Pb$	$^{238}U/^{204}Pb$
ASb (Amphibole skarn)							
ASb-1	Apatite > 125 μm	12	2.2	33.192	16.480	40.641	430
ASb-2	Apatite 125–100 μm	30	43	23.068	15.864	40.442	48.6
ASb-3	Apatite < 100 μm	45	40	25.448	15.987	41.225	81.3
ASb-5	Amphibole	0.80	17	18.504	15.634	38.422	2.97
HAS1 (Amphibole skarn)							
HAS1-1	Apatite	0.56	6.7	18.427	15.605	38.505	5.34
HAS1-3	Amphibole	2.2	9.9	18.725	15.632	38.876	14.3
HAS3 (Amphibole skarn)							
HAS3-1	Apatite > 125 μm	0.27	0.93	19.091	15.700	39.208	19.1
HAS3-2	Apatite 125–100 μm	3.2	6.1	21.629	15.819	39.980	35.9
HAS3-3	Apatite < 100 μm	1.5	3.0	19.714	15.747	34.612	31.2
HAS3-4	Amphibole	0.72	1.4	20.916	15.738	39.122	34.3
HGS2 (Garnet skarn)							
HGS2-1	Apatite	0.25	3.5	18.534	15.682	38.726	4.51
HGS2-2	Feldspar	0.89	3.0	19.080	15.625	38.556	18.9
HGS2-3	Garnet	0.41	2.4	18.623	15.333	36.356	10.5
HMS1 (magnetite skarn)							
HMS1-1	Apatite > 125 μm	0.059	1.7	18.647	15.648	38.831	2.21
HMS1-2	Apatite < 125 μm	0.39	4.7	18.562	15.616	38.421	5.20
HMS1-3	Feldspar	0.022	1.2	18.877	15.874	39.125	1.15
HMS1-4	Sulfides	0.0087	872	18.365	15.613	38.334	< 0.001

At Hämmerlein, cassiterite is paragenetic with secondary chlorite, fluorite, tourmaline, and locally also with a second generation of fine-grained ferroan poly-lithionite, i.e., a texturally late generation, with overprint-related minerals that have not been used to constrain the Rb-Sr ages. Actually, the Rb-Sr isotope systematics of the few analyzed secondary minerals clearly show anomalously high $^{87}Sr/^{86}Sr$ values. It is unclear from textural observations whether these secondary minerals formed in a retrograde phase during regional metamorphism, i.e., whether they are temporally close to the dated peak assemblage, or formed during a second, unrelated and distinctly younger event, in connection to the emplacement of the Eibenstock granite at c. 320 Ma.

Among the analyzed secondary minerals, fluorite from the pyroxene skarn (sample CSV1) and blue fluorite and apatite from the amphibole skarn (sample HAS3) have particularly high $^{87}Sr/^{86}Sr$ ratios and very low $^{87}Rb/^{86}Sr$ ratios. To highlight the contrast of Sr isotopic signatures between these two fluorite and the apatite samples and the other minerals used to date the skarn, $^{87}Sr/^{86}Sr$ isotopic ratio of all mineral fractions has been recalculated from the measured value to their initial value at 341.2 ± 3.8 Ma for the pyroxene skarn (Fig. 12a) and at 337.0 ± 3.9 Ma for the amphibole skarn (Fig. 12b). The reduced isochron diagrams with initial $^{87}Sr/^{86}Sr$ vs $^{87}Rb/^{86}Sr$ show that all mineral fractions are, considering the uncertainty intervals, on the initial isochron with a $^{87}Sr/^{86}Sr$ of 0.724 for the pyroxene skarn and 0.729 for the amphibole skarn, except the fluorite fraction ($^{87}Sr/^{86}Sr_{341.2\ Ma} = 1.0558$) and apatite ($^{87}Sr/^{86}Sr_{337.0\ Ma} = 0.93492$) of the pyroxene skarn and blue fluorite ($^{87}Sr/^{86}Sr_{337.0\ Ma} = 1.2715$) of the amphibole skarn. Thus, these minerals have acquired their radiogenic Sr isotopic compositions at a time different from the time of skarn formation. Using the initial $^{87}Sr/^{86}Sr$ of the isotopic compositions of skarn samples CSV1 and HAS3 and the initial $^{87}Sr/^{86}Sr$ of the Eibenstock granite (all below 0.73) as estimates of the Sr isotopic composition available for redistribution at the time of the skarn formation and as estimates of the Sr released from the granite, respectively, it is obvious that fluorite and apatite received Sr from a different source. One possible source includes high $^{87}Rb/^{86}Sr$ minerals that had developed high $^{87}Sr/^{86}Sr$ at the time they were destabilized during fluorite formation. For instance, biotite and muscovite were consumed during the formation of chlorite. Biotite and muscovite (Fig. 12) have very high $^{87}Rb/^{86}Sr$ ratios and thus may develop markedly radiogenic $^{87}Sr/^{86}Sr$ ratios within a short period of only a few million years. The minimum duration of time elapsed between the time of biotite formation and biotite alteration can be roughly estimated using the following assumptions: (i) biotite is the dominant source for the Sr in fluorite and apatite; (ii) the highest $^{87}Rb/^{86}Sr$ among skarn

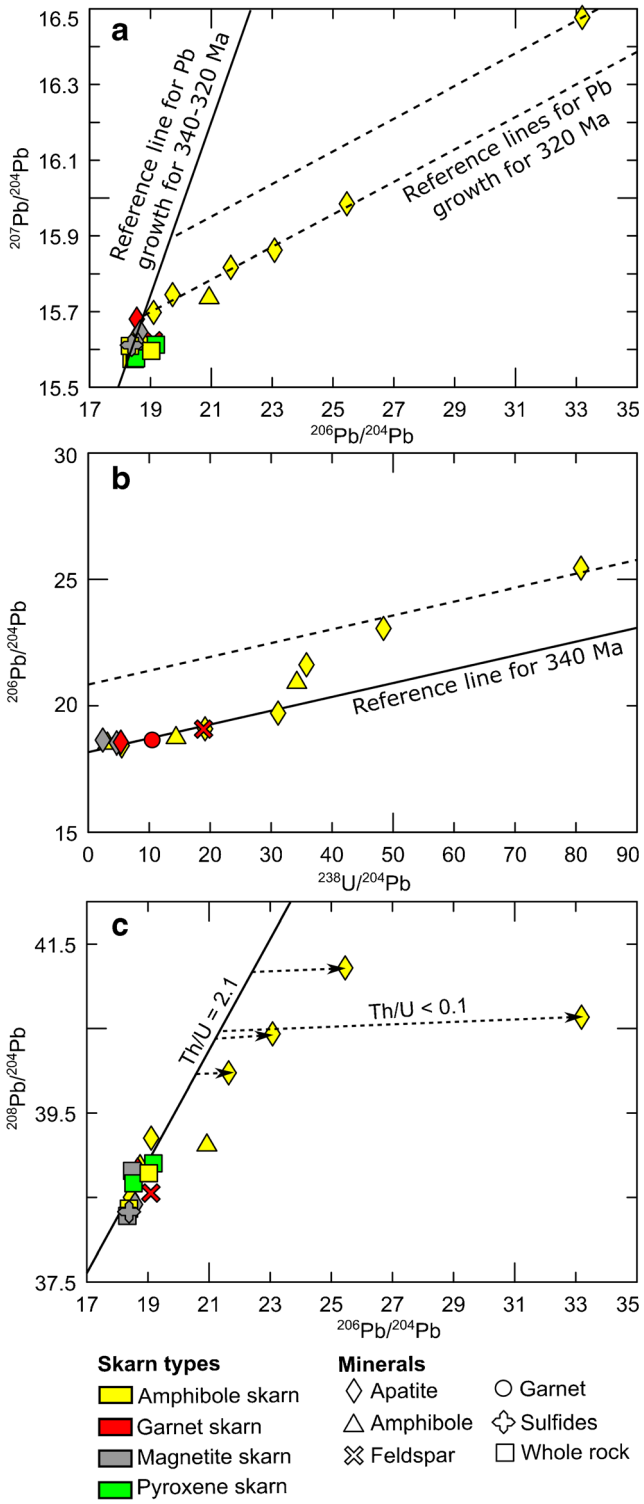

Fig. 11 $^{207}Pb/^{204}Pb$ vs $^{206}Pb/^{204}Pb$ (a), $^{206}Pb/^{204}Pb$ vs $^{238}U/^{204}Pb$ (b), and $^{208}Pb/^{204}Pb$ vs $^{206}Pb/^{204}Pb$ (c) diagrams for skarn samples from the Hämmerlein deposit. Minerals data: see Table 5, whole rocks data: unpublished data

minerals is a good estimate for the $^{87}Rb/^{86}Sr$ of the mineral that serves as Sr source for the Sr in fluorite and apatite; and (iii) the initial $^{87}Sr/^{86}Sr$ of the skarn assemblage represents a good estimate of the initial $^{87}Sr/^{86}Sr$ of biotite. Using 0.7241 as $^{87}Sr/^{86}Sr$ initial for the skarn, 1.056 for the fluorite, and 1900 as $^{87}Rb/^{86}Sr$ estimated for the biotite, the gap between skarn formation and fluorite crystallization is estimated to be about 20 million years. Additions of Sr derived from minerals with lower $^{87}Rb/^{86}Sr$ actually would require a longer gap between the formation of the skarn and the formation of secondary fluorite and apatite. A shorter duration, however, would be obtained if the Sr source for Sr in fluorite had an even higher $^{87}Rb/^{86}Sr$ than assumed for the above estimate. For instance, to obtain a gap of only 2 Ma, fluorite would have to have a $^{87}Rb/^{86}Sr$ ratio as high as 40,000, which is very unlikely even for mineralized skarn systems. For instance, the highest $^{87}Rb/^{86}Sr$ among the here dated mica fractions from greisen samples is c. 19,300 (Table 5, Fig. 10) and greisen represent a system that generally develops a much higher $^{87}Rb/^{86}Sr$ than skarns. Therefore, fluorite, apatite, and texturally related minerals (albite, chlorite, tourmaline, secondary muscovite, and cassiterite) are not related to the process of formation of the skarn, but instead are related to a second unrelated event of retrogression. This second event could well be the emplacement of the Eibenstock granite at c. 320 Ma. Such a two-stage process of skarn and mineralization formation also is known from the Big Bell gold skarn (Australia) that shows a pre-granite skarn with one mineralization before the granite intrusion, and another mineralization after the granite intrusion (Mueller et al. 1996; Mueller and McNaughton 2000).

A two-stage Pb growth also highlights two stages for skarn formation. The two stages have to be separated in time to explain the observed isotopic compositions. Similar as for Sr in apatite and fluorite, the two stages could be (i) the development between the regional metamorphism and the emplacement of the granites and (ii) post-granite Pb development. During the first stage between c. 340 and c. 320 Ma, apatite and amphibole with high $^{238}U/^{204}Pb$ developed higher $^{206}Pb/^{204}Pb$ and $^{207}Pb/^{204}Pb$ than the other minerals of the skarn. For the second stage at c. 320 Ma, the fluid derived from the Eibenstock and related granites induced either the loss of U and Th from apatite and amphibole or the incorporation of radiogenic Pb by apatite and amphibole.

Hämmerlein—a skarn with two events of Sn mineralization

Isotopic dating of the mineral assemblage of the amphibole skarn (Fig. 10) and the anomalous Sr and Pb isotopic composition of retrograde minerals associated with cassiterite (Figs. 11 and 12) in combination with the enhanced Sn contents in skarn minerals demonstrate that there are two stages of Sn introduction into the Hämmerlein skarn deposit. Tin related to the first stage is economically irrelevant as it is bound to silicate minerals and does not form a phase of its own. In

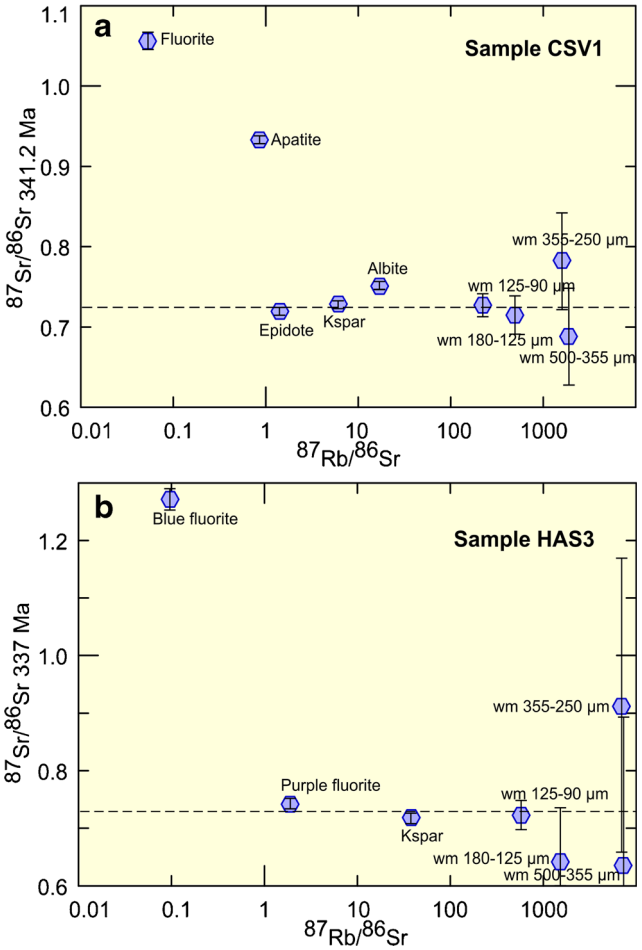

Fig. 12 Rb-Sr reduced isochron diagrams of the pyroxene skarn (sample CSV1) and the amphibole skarn (sample HAS3). Samples that do not fall within uncertainties on the dashed lines (reduced isochrones) are in isotopic disequilibrium with the mineral assemblage which defines the age. Note the extremely radiogenic Sr isotopic composition of fluorite in sample CSV1 and of blue fluorite in sample HAS3. Such high ratios require a Sr source that has a very high $^{87}Sr/^{86}Sr$ and that aged for some time. Pyroxene and amphibole skarn Rb-Sr mineral data have been recalculated to the age of initial assemblage formation, i.e., 341.2 and 337.0 Ma, respectively

contrast, Sn related to the second stage is mostly bound to cassiterite and, therefore, economically interesting.

The first tin enrichment corresponds to the tin-bearing calc-silicate minerals that crystallized during the skarn formation. Therefore, these minerals are directly associated with the c. 340-Ma regional metamorphism ,which affected the Cambro-Ordovician volcanosedimentary rocks. One likely scenario for the first tin enrichment is, upon heating (up to 400–450 °C) during the Variscan metamorphism, the Cambro-Ordovician volcanosedimentary rocks may have released fluids, which were able to mobilize Sn from the sedimentary rocks and to form Sn (II) chloride complexes (Schmidt 2018). Those complexes reacted with the carbonate layers within the sedimentary units, increasing XCO_2 of the fluid (Schmidt 2018). In units containing more carbonates, XCO_2 was higher, stabilizing garnet skarn. Amphibole and pyroxene skarns formed at lower XCO_2, possibly reflecting either a lower carbonate content or that the actually reacting rocks already had partially been decarbonated. The release of CO_2 due to fluid-rock interaction destabilized Sn-complexes in the fluid (Schmidt 2018). Sn was incorporated into garnet, amphibole, and pyroxene by substituting for Fe^{2+} (McIver and Mihálik 1975), Mg^{2+} or Ca^{2+} (De Vore 1955), or as SnO_4^{4-} that may substitute for SiO_4^{4-} (Dadàk and Novák 1965), resulting in Sn-rich skarn silicates.

Cassiterite in the skarn, which formed during a second stage mineralization, occurs mostly in the amphibole skarn, typically in association with chlorite, and in the greisen, forming cassiterite-chlorite-fluorite-tourmaline assemblages. The systematic cassiterite-chlorite association both in skarn and greisen may indicate that chloritization of biotite and amphibole is the likely cause of destabilization of Sn complexes in the hydrothermal fluid. The acidic fluids derived from the Eibenstock granite altered biotite and to a lesser extent amphibole. Formation of chlorite at the expense of biotite releases Fe and Sr. The latter is distinctive by its highly radiogenic composition (because of the high $^{87}Rb/^{86}Sr$ of the precursor biotite) and eventually becomes incorporated into newly formed fluorite with remarkably high initial $^{87}Sr/^{86}Sr$ ratios (Fig. 12). Iron released in the skarn and greisen mineralization may form complexes with Cl ($FeCl_2$ or $FeCl_3$) and, thus, compete with Sn for Cl as ligand. As the formation of Fe-chlorides is energetically more favorable than that of Sn-chlorides (Sukhoruchkin and Soroko 2009a, b) and there is much more Fe in the system than Sn, Cl-ligands are mostly bound to Fe, which eventually implies that Sn precipitates as cassiterite in skarn and greisen. Biotite could also have released Sn into the system as described by Johan et al. (2012). This retraction of Cl-ligands could have caused an oversaturation of tin in the fluid, which would have resulted in the precipitation of cassiterite.

Acknowledgments We thank Saxore Bergbau GmbH for providing access to the outcrops and samples. We thank Bettina Hübner for her support during the chemical preparation of the samples, and Franziska Wilke and Oona Appelt for their help during EPMA analysis.

Funding information This project was supported by the German Government BMBF grant 033R134A awarded to RLR.

References

Anglo Saxony Mining (2015) Westerzgebirge project Hämmerlein-Tellerhäuser: long section through adit. http://www.anglosaxony.com/projects/germany/tellerhauser. Accessed 04 June 2018

Brady J, Perkins D (2015) Mineral formulae recalculation. SERC Carleton College http://serc.carleton.edu/research_education/equilibria/mineralformulaerecalculation.html. Accessed 31 May 2017

Breiter K (1993) The Nejdek pluton—discussion of granite evolution and Sn-W mineralization. Z Geol Wissenschaft 21:2–36

Breiter K (2012) Nearly contemporaneous evolution of the A- and S-type fractionated granites in the Krušné hory/Erzgebirge Mts., Central Europe. Lithos 151:105–121

Breiter K, Förster HJ, Seltmann R (1999) Variscan silicic magmatism and related tin-tungsten mineralization in the Erzgebirge-Slavkoský les metallogenic province. Mineral Deposita 34:505–521

Dadàk V, Novák F (1965) Tin-containing andradite from Plavno mine in the Krušné Hory Mts., Czechoslovakia. Mineral Mag 35:379–385

deCapitani C, Petrakakis K (2010) The computation of equilibrium assemblage diagrams with Theriak/Domino software. Am Mineral 95: 1006–1016

de Vore GW (1955) The rate of adsorption in the fractionation and distribution of elements. J Geol 63:159–190

Diamond LW (2001) Review of the systematics of CO_2-H_2O fluid inclusions. Lithos 55:69–99

Förster B (1996) U/Pb Datierung an Pechblenden der U-Lagerstätte Aue-Niederschlema (Erzgebirge). Ph.D. Thesis, University of Giessen, Germany

Förster HJ (1998) Die variszischen Granite des Erzgebirge und ihre akzessorischen Minerale. Habilitation Thesis, Tech Univ Bergakademie Freiberg, Germany

Förster HJ, Romer RL (2010) Carboniferous magmatism. In: Linnemann U, Romer RL (eds) Pre-Mesozoic geology of Saxo-Thuringia—from the Cadomian active margin to the Variscan orogen, 1st edn. Schweizerbart, Stuttgart, pp 287–308

Förster HJ, Tischendorf G, Trumbull RB, Gottesmann B (1999) Late-collisional granites in the Variscan Erzgebirge, Germany. J Petrol 40:1613–1645

Franke W (1989) Tectonostratigraphic units in the Variscan belt of central Europe. Geol Soc Spec Pap 230:67–90

Glodny J, Bingen B, Austrheim H, Molina JF, Rusin A (2002) Precise eclogitization ages deduced from Rb/Sr mineral systematics: the Maksyutov complex, Southern Urals, Russia. Geochim Cosmochim Acta 66:1221–1235

Hawthorne FC, Dirlam DM (2011) Tourmaline the indicator mineral: from atomic arrangement to viking navigation. Elements 7:307–312

Heinrich W (2007) Fluid immiscibility in metamorphic rocks. Rev Mineral Geochem 65:389–430

Johan Z, Strnad L, Johan V (2012) Evolution of the Cínovec (Zinnwald) granite cupola, Czech Republic: composition of feldspars and micas, a clue to the origin of W, Sn mineralization. Can Mineral 50:1131–1148

Kempe U, Bombach K, Matukov D, Schlothauer T, Hutschenreuter J, Wolf D, Sergeev S (2004) Pb/Pb and U/Pb zircon dating of subvolcanic rhyolite as a time marker for Hercynian granite magmatism and Sn mineralization in the Eibenstock granite, Erzgebirge, Germany: considering effects of zircon alteration. Mineral Deposita 39:646–669

Kroner U, Hahn T, Romer RL, Linnemann U (2007) The Variscan orogeny in the Saxo-Thuringian zone–heterogenous overprint of Cadomian/Paleozoic Peri-Gondwana crust. Geol S Am S 423: 153–172

Kroner U, Romer RL (2013) Two plates—many subduction zones: the Variscan orogeny reconsidered. Gondwana Res 24:298–329

Kroner U, Roscher M, Romer RL (2016) Ancient plate kinematics derived from the deformation pattern of continental crust: Paleo- and Neo-Tethys opening coeval with prolonged Gondwana-Laurussia convergence. Tectonophysics 681:220–233

Kröner A, Willner AP, Hegner E, Frischbutter A, Hofmann J, Bergner R (1995) Latest Precambrian (Cadomian) zircon ages, Nd isotopic systematics and P-T evolution of granitoid orthogneisses of the Erzgebirge, Saxony and Czech Republic. Geol Rundsch 84:437–456

Leake BE, Wooley AR, Arps CES, Birch WD, Gilbert MC, Grice JD, Hawthorne FC, Kato A, Kisch HJ, Krivovichev VG, Linthout K, Laird J, Mandarino JA, Maresch WV, Nickel EH, Rock NMS, Schumacher JC, Smith DC, Stephenson NCN, Ungaretti L, Whittaker EJW, Youzhi G (1997) Nomenclature of amphiboles: report of the subcommittee on amphiboles of the international mineralogical association commission on new minerals and minerals names. Can Mineral 35:219–246

Lefebvre MG, Romer RL, Glodny J, Roscher M (2017) Two stages of skarn formation in the Hämmerlein tin-skarn deposit, western Erzgebirge, Germany. 14th SGA Bienn Meet 4:1305–1308

Leonhardt D, Geißler E, Engelhardt-Sobe A, Baumgart G (2004) Geologische Karte des Freistaates Sachsen 1:25000. Blatt 5542 Johanngeorgenstadt. Sächsisches Landesamt für Umwelt und Geologie Abteilung Geologie (ed)

Leonhardt D, Geißler E, Engelhardt A, Baumgart G. (2010) Geologische Karte des Freistaates Sachsen 1:25000. Blatt 5541 Eibenstock. Sächsisches Landesamt für Umwelt und Geologie Abteilung Geologie (ed)

Leonhardt D, Geißler E, Fritzsche H (1999) Geologische Karte des Freistaates Sachsen 1:25000. Blatt 5543 Oberwiesenthal. Sächsisches Landesamt für Umwelt und Geologie Abteilung Geologie (ed)

Linnemann U, McNaughton NJ, Romer RL, Gehmlich M, Drost K, Tonk C (2004) West African provenance for Saxo-Thuringia (Bohemian Massif): did Armorica ever leave pre-Pangean Gondwana?—U/Pb-SHRIMP zircon evidence and the Nd-isotopic record. Int J Earth Sci 93:683–705

Malyshev BI, Korzhanovskaya VS (1989) Behavior of tin in calcareous-skarn and greisen processes. Geokhimiya 2:216–226

Malyshev BI, Mironova OF, Naumov VB, Savel'eva NI, Salazkin AN, Volosov AG (1997) Fluids of the Hemmerlein Skarn-Greisen tin deposit, Erzgebirge, Germany. Geokhimiya 1:179–188

Matte P (1986) Tectonics and plate tectonics model for the Variscan belt of Europe. Tectonophys 126:329–374

McIver JR, Mihálik P (1975) Stannian andradite from "Davib Ost", South West Africa. Can Mineral 13:217–221

Mingram B (1998) The Erzgebirge, Germany, a subducted part of northern Gondwana: geochemical evidence for repetition of early Palaeozoic metasedimentary sequences in metamorphic thrust units. Geol Mag 135:785–801

Mueller AG, McNaughton NJ (2000) U-Pb ages constraining batholith emplacement, contact metamorphism, and the formation of gold and W-Mo skarns in the southern cross area, Yilgarn craton, Western Australia. Econ Geol 95:1231–1257

Mueller AG, Campbell IH, Schiøtte L, Sevigny JH, Layer PW (1996) Constraints on the age of granitoid emplacement, metamorphism, gold mineralization, and subsequent cooling of the Archean greenstone terrane at Big Bell, Western Australia. Econ Geol 91:896–915

Rojík P (2005) Tin deposits at Přebuz and Rolava in the Krušné hory/Erzgebirge, Czech Republic: classic localities, new challenges. J Czech Geol Soc 50:157–165

Romer RL, Hahne K (2010) Life of the Rheic Ocean: scrolling through the shale record. Gondwana Res 17:236–253

Rötzler K, Plessen B (2010) The Erzgebirge: a pile of ultrahigh- to low-pressure nappes of Early Paleozoic rocks and their Cadomian basement. In: Linnemann U, Romer RL (eds) Pre-Mesozoic geology of Saxo-Thuringia—from the Cadomian active margin to the Variscan Orogen. Schweizerbart, Stuttgart, pp 253–270

Rötzler K, Schumacher R, Maresch W, Willner A (1998) Characterization and geodynamic implications of contrasting metamorphic evolution in juxtaposed high-pressure units of the western Erzgebirge (Saxony, Germany). Eur J Mineral 10:261–280

Schmidt C (2018) Formation of hydrothermal tin deposits: Raman spectroscopic evidence for an important role of aqueous Sn (IV) species. Geochim Cosmochim Acta 220:499–511

Schuppan W, Hiller A (2012) Die Komplexlagerstätten Tellerhäuser und Hämmerlein. Bergbaumonografie, Freiberg Band 17:162p

Selway J, Xiong J (2015) Tourmaline recalculation: developed by Julie Selway & Jian Xiong. Andy Tindle—Free Software. http://www.open.ac.uk/earth-research/tindle/AGTWebPages/AGTSoft.html. Accessed 31 May 2017

Shapenko VV, Šmidel P (1991) Sn and W mineralization in skarn-greisen deposits at the northern margin of the Bohemian massif. Geokhimiya 5:724–732

Štemprok M, Blecha V (2015) Variscan Sn-W-Mo metallogeny in the gravity picture of the Krušné hory/Erzgebirge granite batholith (Central Europe). Ore Geol Rev 69:285–300

Sukhoruchkin SI, Soroko ZN (2009a) Atomic mass and nuclear binding energy for Fe-56 (Iron). In: Schopper H (ed) Landolt-Börnstein—group I elementary particules, nuclei and atoms. Springer, Berlin Heidelberg, pp 2276–2278

Sukhoruchkin SI, Soroko ZN (2009b) Atomic mass and nuclear binding energy for Sn-119 (tin). In: Schopper H (ed) Landolt-Börnstein—group I elementary particules, nuclei and atoms. Springer, Berlin Heidelberg, pp 6838–6840

Tichomirowa M, Hofmann M, Schaltegger U, Sergeev S, von Quadt A, Whitehouse M (2016) The "older" and "younger" granites from the western Erzgebirge—comparison of different zircon dating methods. Freib Online Geosci 46:36–38

Tichomirowa M, Leonhardt D (2010) New age determinations (Pb/Pb zircon evaporation, Rb/Sr) on the granites from Aue-Schwarzenberg and Eibenstock, western Erzgebirge, Germany. Z Geol Wiss 38:99–123

Tischendorf G, Gottesmann B, Förster H-J, Trumbull RB (1997) On Li-bearing micas: estimating Li from electron microprobe analyses and an improved diagram for graphical representation. Mineral Mag 61(409):809–834

Tischendorf G, Förster HJ, Gottesmann B (2001) Minor and trace-element composition of trioctahedral micas: a review. Mineral Mag 65:249–276

Velichkin VI, Chernyshov IV, Simonova LI, Yudintsev SV (1994) Geotectonic position, petrochemical and geochronological features of the Younger Granite Complex in the Krŭsné Hory (Erzgebirge) of the Bohemian massif. J Czech Geol Soc 39:116

Wang L, Shimazaki H, Wang J, Wang Y (2001) Ore-forming fluid and metallization of the Huanggangliang skarn Fe-Sn deposit, Inner Mongolia. Sci China Ser D 44:735–747

Wang RC, Xie L, Chen J, Yu A, Wang LB, Lu JJ, Jinchu Zhu JC (2013) Tin-carrier minerals in metaluminous granites of the western Nanling Range (southern China): constraints on processes of tin mineralization in oxidized granites. J Asian Earth Sci 74:361–372

Wenzel T, Mertz DF, Oberhänsli R, Becker T, Renne PR (1997) Age, geodynamic setting, and mantle enrichment processes of a K-rich intrusion from the Meissen massif (northern Bohemian massif) and implications for related occurrences from the mid-European Hercynian. Geol Rundsch 86:556–570

Werner O, Lippolt HJ (2000) White mica 40Ar/39Ar ages of Erzgebirge metamorphic rocks simulating the chronological results by a model of Variscan crustal imbrication. In: Franke W, Haak V, Oncken O, Tanner D (eds) Orogenic processes: quantification and modelling in the Variscan belt of Central Europe. Geol Soc Lond Spec Publ 179: 323–336

Willner A, Rötzler K, Maresch W (1997) Pressure-temperature and fluid evolution of quartzo-feldspathic rocks with a relic high-pressure, granulite-facies history from the central Erzgebirge (Saxony, Germany). J Petrol 38:307–336

Zhao KD, Jiang SY, Jiang YH, Wang RC (2005) Mineral chemistry of the Qitianling granitoid and the Furong tin ore deposit in Hunan Province, South China: implication for the genesis of granite and related tin mineralization. Eur J Mineral 17:635–648